International Journal of Photoenergy

Nanomaterials for Photocatalysis and Applications in the Environment

Lead Guest Editor: Jinliang Li
Guest Editors: Guang Zhu and Muhammad S. Javed

Nanomaterials for Photocatalysis and Applications in the Environment

International Journal of Photoenergy

Nanomaterials for Photocatalysis and Applications in the Environment

Lead Guest Editor: Jinliang Li
Guest Editors: Guang Zhu and Muhammad S. Javed

Chief Editor

Academic Editors

Contents

Hindawi
International Journal of Photoenergy
Volume 2020, Article ID 4756952, 6 pages
https://doi.org/10.1155/2020/4756952

Research Article

SiO_2-TiO_2 Films Supported on Ignimbrite by Spray Coating for the Photocatalytic Degradation of NO_x Gas and Methyl Orange Dye

Daily Maria Magdalena Gallegos Florez,[1] **Rivalino Benicio Guzman Ale**,[1] **Albeniz Ferdinand Huaracallo Idme**,[1] **Luis Antonio Lazo Alarcon**,[1] **Edgar Apaza Huallpa**,[1] **Yolanda Castro**,[2] **Pierre Giovanny Ramos Apestegui**,[3] **and Juan Martin Rodriguez Rodriguez**[3]

[1]*Universidad Nacional de San Agustín de Arequipa, Peru*
[2]*Institute of Ceramics and Glass-CSIC-Madrid, Spain*
[3]*Center for the Development of Advanced Materials and Nanotechnology, Universidad Nacional de Ingeniería, Av. Túpac Amaru, 210 Lima, Peru*

Correspondence should be addressed to Daily Maria Magdalena Gallegos Florez; dgallegosf@unsa.edu.pe

Received 17 October 2019; Revised 5 November 2019; Accepted 6 November 2019; Published 29 January 2020

Guest Editor: Jinliang Li

In this work, a SiO_2-TiO_2 coating, composed of different numbers of TiO_2 and SiO_2 layers, was fabricated by a spray-coating technique. The films were deposited onto ignimbrite rock and divided into two groups according to the number of SiO_2 layers applied, 10 and 15 layers of SiO_2 and 5 layers of TiO_2 for each group. The morphology and chemical composition of the synthesized samples were characterized by field emission scanning electron microscopy (FE-SEM) and energy dispersive X-ray spectrometer (EDS), which reveal the successful SiO_2-TiO_2 coating on ignimbrite. The photocatalytic activities of samples obtained were evaluated toward the decomposition of 3 ppm of methyl orange (MO). Finally, NO_x gas degradation was studied. The obtained results evidenced that the SiO_2 and TiO_2 coating improved the photocatalytic activity of ignimbrite.

1. Introduction

In Peru, there are few studies on mitigating damage to rocks belonging to architectural monuments. However, in the city of Lima, Gallarday [1] studied the deterioration of various churches in the historic center of the city and made a financing proposal for the preservation and restoration of the main ornamental rocks. In Arequipa, the most important study was carried out in 2006 [2] by the Ministry of the Environment, in which the main agents and mechanisms of alteration of the rocks (ignimbrite) belonging to the historical monuments of Arequipa were determined. Thanks to this study, the concern for the improvement of the historic center of Arequipa city began, seeking effective and simple solutions or alternative that allows the protection, self-cleaning, and preservation of the cultural heritage. In this aspect, the use of nanomaterials begins to gain importance to achieve the desired improvement. Zornosa-Indart et al. [3, 4] used silica-based inorganic hybrid nanomaterials that improve robustness, hydrophobicity, and resistance and consolidate limestone rocks significantly, in order to achieve the conservation of the cultural heritage. Additionally, the use of titanium dioxide (TiO_2) photocatalyst in the improvement of the facades of historic buildings has been studied with good results [5, 6] and in combination with cementitious and other construction materials has shown a favorable synergetic effect in the removal of air pollutants [7, 8]. Thus, the researches continued and led to the implementation of a system based on silica as a support material and TiO_2 nanoparticles as a photocatalyst material [9–11]. Nevertheless, the use of a silicon-titanium hybrid system in the degradation of methyl orange (MO) dye and NO_x gases on ignimbrite surfaces has not yet been reported. Therefore, the aim of this work is to carry out a study on a TiO_2-SiO_2 coating system,

(a) (b) (c)

Figure 1: Photographs of (a) ignimbrite, (b) 10TEOS-5TiO_2, and (c) 15TEOS-5TiO_2 samples.

composed of different numbers of layers of SiO_2 and TiO_2 achieved with the spraying coating technique. These coatings could protect the cultural heritage of the city of Arequipa, Peru, from organic and air pollutants. Detailed morphological characterization of samples was investigated by field emission scanning electron microscopy (FE-SEM). Then, methyl orange dye degradation measurements will be previously performed in order to determine the effectiveness of the coating systems. Finally, we will evaluate the NO_x gas elimination capacity in a laboratory gas analyzer.

2. Experimental

2.1. Synthesis of the Sols. All reagents used in the experiments were of analytical grade and used without any further purification. The TiO_2 and SiO_2 sols were prepared, respectively, according to Arconada [12] and Reyes et al. [13]. The TiO_2 sol was obtained from the mixture of 49.5426 g of ethanol, component used as solvent of the sol-gel process with 1.6140 g of acetic acid and 7.8758 g of titanium isopropoxide (TTIP), where TTIP is the main component of titanium precursor. Then, 0.9676 g of water acidified with hydrochloric acid (HCl, 0.1 N), that acts as the catalyst for the solution, was added dropwise, and the whole mixture was stirring for 1 hour until dissolved. Meanwhile, the preparation of the silica sol (SiO_2) was prepared from the precursor tetraethylorthosilicate (TEOS), dissolving 40.602222 g of TEOS in 105.63776 g of ethanol. Then, 3.4384 g of water acidified with 0.1 N hydrochloric acid was added dropwise; the mixture was stirring at 60°C in a cooling bath with glycerin at 11°C for a period of 90 minutes. After that time, the temperature was reduced to 40°C and 10.31536 g of acidified water was added dropwise again. Finally, the solution was left under stirring for a period of 60 minutes in the cooling bath.

2.2. Deposition of the Coatings. The coating of ignimbrite employing TiO_2 and SiO_2 sols was carried out by a spray-coating technique, using a set of airbrushes with fluid control at a distance of 5 cm from the ignimbrite. SiO_2 and TiO_2 layers were obtained by calcination at 450°C for 30 minutes and 60 minutes, respectively, at a heating rate of 10°C/min. Two groups of samples were fabricated according to the number of layers of TiO_2 and SiO_2 applied. The first group of samples was fabricated with 10 layers of SiO_2 and 5 of TiO_2 and labelled as 10TEOS-5TiO_2, whereas the second group was fabricated with 15 layers of SiO_2 and 5 of TiO_2 and labelled as 15TEOS-5TiO_2.

2.3. Characterization of the Samples. The morphologies of obtained samples were visualized by a field emission scanning electron microscope (FESEM, Hitachi Regulus 8230) equipped with an energy dispersive X-ray spectrometer

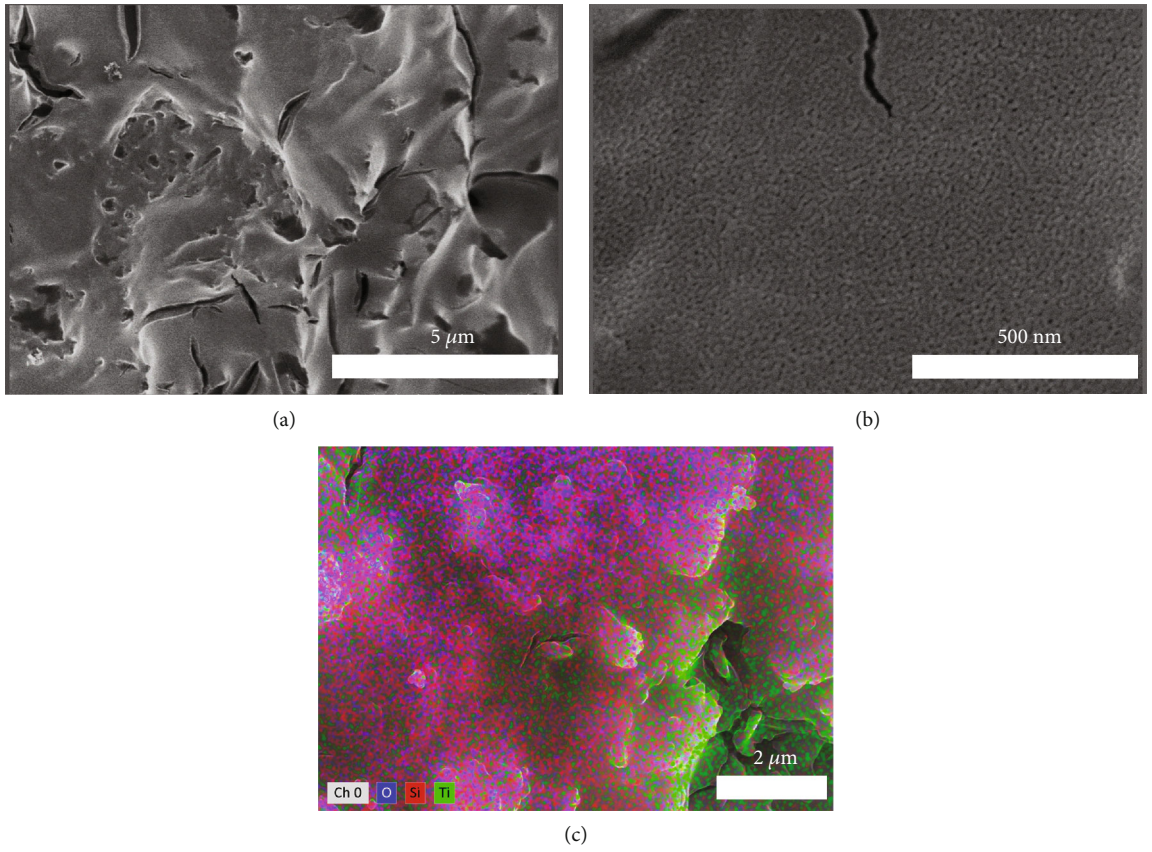

(a) (b) (c)

FIGURE 2: FE-SEM images of 15TEOS-5TiO_2 samples at magnification of (a) 10 KX and (b) 80 KX. (c) EDS element mapping image.

(EDX). The photocatalytic activities of the fabricated nanostructures were evaluated by the degradation of methyl orange (MO) under UV light irradiation, using a light source which simulates solar radiation (Newport 50-500 W). The next step was NO_x gas mitigation monitoring ($NO+NO_2$) performed with a chemiluminescence analyzer AC-32 M, Environment S.A., following the guidelines of ISO 22197-1: 2007. The NO_x degradation efficiency was calculated using

$$\%NO_x = \frac{[NO_x]_{in} - [NO_x]_{out}}{[NO_x]_{in}} \times 100, \quad (1)$$

where $[NO_x]_{in}$ is the initial NO_x concentration (before turning on the UV source) and $[NO_x]_{out}$ is the concentration at the end of the illumination period.

The photocatalytic activity and NO_x degradation of 10TEOS-5TiO_2 and 15TEOS-5TiO_2 samples fabricated by a spray-coating technique were compared.

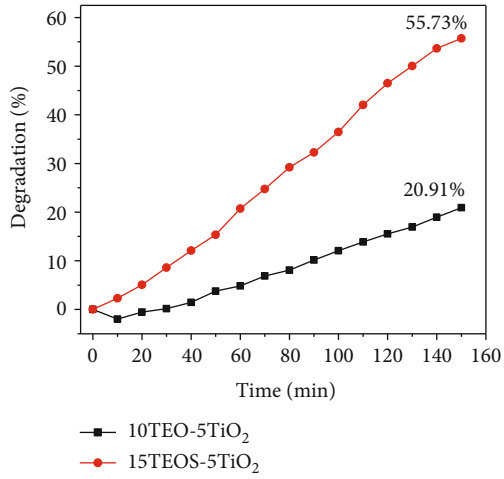

FIGURE 3: Photodegradation curves of methyl orange with different photocatalyst: 10TEOS-5TiO_2 (black line) and 15TEOS-5TiO_2 (red line).

3. Results and Discussion

Figure 1 shows a photograph of ignimbrite, 10TEOS-5TiO_2, and 15TEOS-5TiO_2 samples. Figure 1(a) is clearly to see the variety of porosity and minerals that conform the ignimbrite, unlike in Figure 1(b) where a whitish color is visualized covering the surface of the rock. In Figure 1(c), the intensity of this color increases and we obtained better compaction of the minerals present in the ignimbrite, an important requirement to be applied on rocks of historical monuments for restoration [14].

The FE-SEM images obtained by field emission scanning electron microscopy of 15TEOS-5TiO_2 samples fabricated by spray coating at magnifications of 10 KX and 80 KX are show in Figures 2(a) and 2(b), respectively. As shown in the figures, TiO_2 layers formed by nanoparticles can been seen in the top

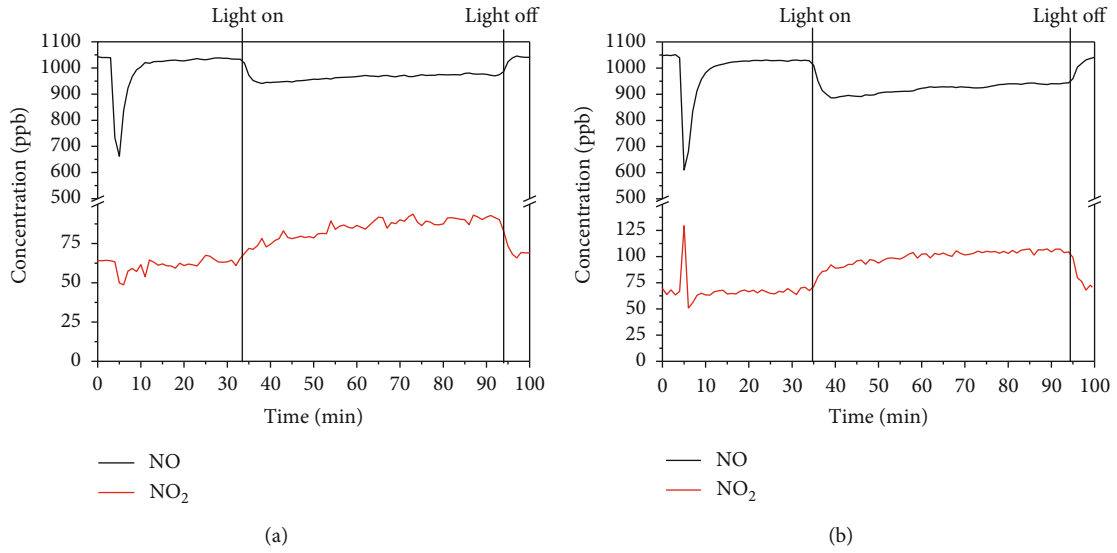

Figure 4: NO and NO_2 concentration during the test according to ISO 22197:1 2007 for (a) 10TEOS-5TiO_2 and (b) 15TEOS-5TiO_2 samples.

of the ignimbrite. Moreover, the EDS element mapping image in Figure 2(c) reveals the presence of titanium (Ti, green), silicon (Si, red), and oxygen (O, blue) elements, proving the coating of SiO_2 and TiO_2 layers on the surface of the ignimbrite.

In order to elucidate the effects of coating with TiO_2 and SiO_2 layers on the ignimbrite, the photocatalytic dye degradation performances of the 10TEOS-5TiO_2 and 15TEOS-5TiO_2 were evaluated in aqueous solution of methyl orange dye under UV-A irradiation. Figure 3(a) shows the change in the methyl orange concentration in aqueous solution in the presence of all samples. As shown, methyl orange molecules were not completely decomposed during 150 min of photocatalytic reaction. However, it was noted that 15TEOS-5TiO_2 photocatalyst shows the highest photocatalytic activity compared with 10TEOS-5TiO_2 photocatalyst. The degradation efficiency of the 15TEOS-5TiO_2 photocatalyst shows a maximum degradation of ~55.73% at 150 min, whereas the degradation efficiency of 10TEOS-5TiO_2 was ~20.91% at the same irradiation time. The enhancement of photocatalytic efficiency must be attributed to the increase in the number of SiO_2 layers, which achieve better support for the coating of TiO_2 [15]. Thus, having more TiO_2 exposed directly the photocatalytic efficiency which could be improved, having a better performance in the degradation of the methyl orange dye.

The chemiluminescence analysis for the variation of the concentration of NO and NO_2 in parts per micromolar is shown in Figure 4. An appropriate amount of the SiO_2-TiO_2-coated ignimbrite was loaded into the reactor, and then, the reactor was carefully sealed. Afterwards, the NO containing nitrogen gas and the purified air were allowed to flow into the reactor at flow rates of 3 L/min each, until equilibrium NO_x concentration in the inflow was achieved (1000 ppb). The evaluation of photocatalytic activity was 1 hour at 10 W/m^2 with 35 minutes of saturation of the rock in the dark. In the first 30 minutes in the dark, the peaks observed in the graphs are the flow of gas entering the chamber, so it has no influence on the measurements. After the one hour of irradiation, the light source was turned off and then the gas valves were closed. All experiments were conducted at ambient temperature (25 ± 3°C). The detailed experimental procedure can be referred to published literatures [7, 8] and the ISO 22197-1 : 2007 standard of air purification performance of semiconductor photocatalytic materials [7]. Figure 4(a) shows a slight increase in NO_2 production for the 10TEOS-5TiO_2 substrate, which causes a greater amount of NO_x removal. In the case of the gaseous medium, a better degradation result of 0.80 μmol was obtained, which translates into 15.95%, whereas the obtained degradation for 15TEOS-5TiO_2 substrate, shown in Figure 4(b), was 0.63 μmol, which is equivalent to 10.56%. According to the reports [16, 17], the NO_x gas degradation phenomena are mainly due to the presence of TiO_2 in our samples.

It is important to know the mechanism of heterogeneous photocatalytic degradation of NO_x gases by TiO_2. These processes are summarized in the following reactions for the 10TEOS-5TiO_2 and 15TEOS-5TiO_2 samples as photocatalytic materials. When the nanostructure is irradiated from the light source, the electrons (e^-) in the valence band (VB) are excited to the conduction band (CB) with generation simultaneous of the same number of holes (h^+) in the VB (Equation (2)).

$$TiO_2 \xrightarrow{+hv} e^-_{CB} + h^+_{VB} \tag{2}$$

The reaction of the H^+ with the OH^- is dissociated from the water to form the OH^* [18–20] and the reaction with the electrons with the O_2 to form a superoxide anion O^{2-} [20, 21].

$$\begin{aligned} h^+_{VB} + H_2O_{ads} &\longrightarrow OH^* + H^+ \\ O_2 + e^-_{CB} &\longrightarrow O_2^{-*} \end{aligned} \tag{3}$$

Then, the reaction of O_2^{-*} with H^+ from water produces HO_2^* radicals; NO diffusion occurs on the surface of TiO_2

and forms NO_2. Finally, NO_2 reacts with hydroxyl radicals forming nitric acid:

$$\begin{aligned} O_2^- + H^+ &\longrightarrow HO_2^* \\ NO + HO_2^* &\longrightarrow NO_2 + OH^* \\ NO_2 + OH^* &\longrightarrow HNO_3 \end{aligned} \quad (4)$$

4. Conclusions

In summary, SiO_2 and TiO_2 coatings on ignimbrite were achieved by a spray-coating technique, varying the number of SiO_2 layers in 10 and 15 layers, while the number of TiO_2 layers remained constant at 5 layers. The photocatalytic activities of the samples obtained were evaluated toward the decomposition of methyl orange (MO) and NO_x gas degradation. The obtained results evidenced that the SiO_2 improved the porosity of ignimbrite, whereas the TiO_2 coating improved the photocatalytic activity. The enhancement in the photocatalytic activity of the SiO_2-TiO_2 hybrid system is attributed to the high efficiency in both light utilizations, the higher transfer rate of photogenerated electrons from SiO_2 to TiO_2 and repressed recombination of the photoinduced hole-electron pairs of TiO_2, which is closely related to the chemical interaction between TiO_2 and SiO_2.

Data Availability

The data used to support the findings of this study are available from the corresponding author upon request.

Conflicts of Interest

The authors declare that they have no conflicts of interest.

Acknowledgments

This work was funded by the Universidad Nacional de San Agustín de Arequipa, with the topic: "Evaluación de Materiales Fotocataliticos y sus Aplicaciones en la Restauracion y Mantenimiento del Patrimonio Cultural de la Ciudad de Arequipa" (No. Contrato IBA 0021-2016) and the collaboration of Eva Jimenez Relinque for her technical assistance in the analysis of NO_x degradation of the Institute of Building Sciences E. Torroja-Madrid. P.G.R.A and J.M.R.R wants to thank the project 32-2019-FONDECYT-BM-INC.INV.

References

[1] T. E. Gallarday, *Mitigación en la alteración de rocas ornamentales debido a efectos ambientales en el Centro Histórico – Lima*, 2014.

[2] G. Ríos, *Estudio de Daños ocasionados por Patologías de la Contaminación Atmosférica*, 2006, Materiales y Monumentos Históricos Arequipa–Perú.

[3] A. Zornoza-Indart, P. Lopez-Arce, J. Simão, and K. Zoghlami, "Consolidation of a Tunisian bioclastic calcarenite: from conventional ethyl silicate products to nanostructured and nanoparticle based consolidants," *Construction and Building Materials*, vol. 116, pp. 188–202, 2016.

[4] A. Zornoza-Indart, P. Lopez-Arce, K. Zoghlami, N. Leal, and J. Simão, "Marine aerosol weathering of Mediterranean calcarenite stone: durability of ethyl silicate, nano $Ca(OH)_2$, nano SiO_2, and nanostructured consolidating products," *Studies in Conservation*, vol. 64, no. 2, pp. 73–89, 2019.

[5] A. A. Mohammad, S. D. Sawsan, A. A. Mahmoud, A. E. Nagib, and M. A. Sayed, "Protecting of marble stone facades of historic buildings using multifunctional TiO_2 nanocoatings," *Sustainability*, vol. 9, no. 11, p. 2002, 2017.

[6] E. Sassoni, E. D'Amen, N. Roveri, G. W. Scherer, and E. Franzoni, "Durable self-cleaning coatings for architectural surfaces by incorporation of TiO_2 nano-particles into hydroxyapatite films," *Materials*, vol. 11, no. 2, p. 177, 2018.

[7] J. A. Mendoza, D. H. Lee, and J.-H. Kang, "Photocatalytic removal of NO_x using TiO_2-coated zeolite," *Environmental Engineering Research*, vol. 21, no. 3, pp. 291–296, 2016.

[8] M. J. Hernández Rodríguez, E. Pulido Melián, O. González Díaz et al., "Comparison of supported TiO_2 catalysts in the photocatalytic degradation of NOx," *Journal of Molecular Catalysis A: Chemical*, vol. 413, pp. 56–66, 2016.

[9] C. Kapridaki, L. Pinho, M. J. Mosquera, and P. Maravelaki-Kalaitzaki, "Producing photoactive, transparent and hydrophobic SiO_2-crystalline TiO_2 nanocomposites at ambient conditions with application as self-cleaning coatings," *Applied Catalysis. B, Environmental*, vol. 156-157, pp. 416–427, 2014.

[10] A. Calia, M. Lettieri, M. Masieri, S. Pal, A. Licciulli, and V. Arima, "Limestones coated with photocatalytic TiO_2 to enhance building surface with self-cleaning and depolluting abilities," *Journal of Cleaner Production*, vol. 165, pp. 1036–1047, 2017.

[11] V. Crupi, B. Fazio, A. Gessini et al., "TiO_2-SiO_2-PDMS nanocomposite coating with self-cleaning effect for stone material: finding the optimal amount of TiO_2," *Construction and Building Materials*, vol. 166, pp. 464–471, 2018.

[12] N. Arconada Gómez-Jareño, *Recubrimientos mesoporosos y mesoestructurados de TiO_2-anatasa por el método sol-gel para aplicaciones en sistemas fotocatalíticos*, 2012.

[13] Y. Reyes, A. Durán, and Y. Castro, "Glass-like cerium sol-gel coatings on AZ31B magnesium alloy for controlling the biodegradation of temporary implants," *Surface and Coatings Technology*, vol. 307, pp. 574–582, 2016.

[14] P. Munafò, G. Batista Goffredo, and E. Quagliarini, "TiO_2-based nanocoatings for preserving architectural stone surfaces: an overview," *Construction and Building Materials*, vol. 84, pp. 201–218, 2015.

[15] I. Alfieri, A. Lorenzi, L. Ranzenigo, L. Lazzarini, G. Predieri, and P. P. Lottici, "Synthesis and characterization of photocatalytic hydrophobic hybrid TiO_2-SiO_2 coatings for building applications," *Building and Environment*, vol. 111, pp. 72–79, 2017.

[16] N. Serpone, "Heterogeneous photocatalysis and prospects of TiO_2-based photocatalytic DeNOxing the atmospheric environment," *Catalysts*, vol. 8, no. 11, p. 553, 2018.

[17] Q. L. Yu, Y. Hendrix, S. Lorencik, and H. J. H. Brouwers, "Field study of NO_x degradation by a mineral-based air purifying paint," *Building and Environment*, vol. 142, pp. 70–82, 2018.

[18] S. Hou, X. Xu, M. Wang, T. Lu, C. Q. Sun, and L. Pan, "Synergistic conversion and removal of total Cr from aqueous solution by photocatalysis and capacitive deionization," *Chemical Engineering Journal*, vol. 337, pp. 398–404, 2018.

[19] X. Liu, B. Liu, L. Li et al., "$Cu_2In_2ZnS_5/Gd_2O_2S$:Tb for full solar spectrum photoreduction of Cr(VI) and CO_2 from UV/vis to near-infrared light," *Applied Catalysis B: Environmental*, vol. 249, pp. 82–90, 2019.

[20] B. Liu, X. Liu, J. Liu et al., "Efficient charge separation between UiO-66 and $ZnIn_2S_4$ flowerlike 3D microspheres for photoelectronchemical properties," *Applied Catalysis B: Environmental*, vol. 226, pp. 234–241, 2018.

[21] B. Liu, X. Liu, L. Li et al., "$CaIn_2S_4$ decorated WS_2 hybrid for efficient Cr(VI) reduction," *Applied Surface Science*, vol. 484, pp. 300–306, 2019.

Hindawi
International Journal of Photoenergy
Volume 2020, Article ID 8740825, 9 pages
https://doi.org/10.1155/2020/8740825

Research Article

Study of the Effect of TiO_2 Layer on the Adsorption and Photocatalytic Activity of TiO_2-MoS_2 Heterostructures under Visible-Infrared Light

N. Cruz-González,[1] O. Calzadilla,[2] J. Roque,[3] F. Chalé-Lara,[4] J. K. Olarte,[5] M. Meléndez-Lira,[6] and M. Zapta-Torres[5]

[1]*CONACYT-Centro de Investigación en Ciencia Aplicada y Tecnología Avanzada, Unidad Legaria, IPN, 11500 Ciudad de México, Mexico*
[2]*Facultad de Física, Universidad de La Habana, 10400 La Habana, Cuba*
[3]*Laboratorio Nacional de Nanoscopía Electrónica-CINVESTAV, 07360 Ciudad de México, Mexico*
[4]*Instituto Politécnico Nacional, CICATA Unidad Altamira, C.P, 89600 Altamira, Tamaulipas, Mexico*
[5]*Instituto Politécnico Nacional, CICATA Unidad Legaria, C.P, 11500 Ciudad de México, Mexico*
[6]*Departamento de Física-CINVESTAV, 07360 Ciudad de México, Mexico*

Correspondence should be addressed to N. Cruz-González; nadiacruzgonzalez@gmail.com

Received 9 November 2019; Accepted 5 December 2019; Published 20 January 2020

Guest Editor: Jinliang Li

In the last decade, the urgent need to environmental protection has promoted the development of new materials with potential applications to remediate air and polluted water. In this work, the effect of the TiO_2 thin layer over MoS_2 material in photocatalytic activity is reported. We prepared different heterostructures, using a combination of electrospinning, solvothermal, and spin-coating techniques. The properties of the samples were analyzed by scanning electron microscopy (SEM), transmission electron microscopy (TEM), atomic force microscopy (AFM), X-ray diffraction (XRD), nitrogen adsorption-desorption isotherms, UV-Vis diffuse reflectance spectroscopy (UV-Vis-DRS), and X-ray photoelectron spectroscopy (XPS). The adsorption and photocatalytic activity were evaluated by discoloration of rhodamine B solution. The TiO_2-MoS_2/TiO_2 heterostructure presented three optical absorption edges at 1.3 eV, 2.28 eV, and 3.23 eV. The high adsorption capacity of MoS_2 was eliminated with the addition of TiO_2 thin film. The samples show high photocatalytic activity in the visible-IR light spectrum.

1. Introduction

The growing need to protect the environment promotes the research of heterogeneous photocatalysis as a "green" technique with great potential to remediate air and water pollution. The photocatalysis process, carried out in the presence of a semiconductor, has the ability of removing organic pollutants and heavy metals from wasted water and air, promoting their mineralization into simpler compounds [1, 2]. Titanium dioxide (TiO_2) is the most investigated semiconductor as an oxidizer organic pollutant in water and air, because it is nontoxic and of relatively low cost [3, 4]. The TiO_2 has three crystalline phases anatase, brookite, and rutile; the photocatalytic activity of anatase is always much higher than rutile [5, 6]. The TiO_2 anatase has a large band gap of 3.2 eV, therefore only absorbs ~3-5% of the solar spectrum; this limits its photocatalytic efficiency due to the low electron mobility and high recombination rate of the photogenerated electron-hole pairs [7]. To shift the absorption edge to the visible region and improve the electron-hole separation, the TiO_2 has been modified with different species such as metal and nonmetal ions, rare earth ions, metal

sulfides, and metal oxides [8–14]. The molybdenum disulfide (MoS_2) is a 2D-layered material; in the bulk, the MoS_2 has a band gap of 1.2 eV located on a near-infrared spectrum [15]. When the MoS_2 is exfoliated to give single- or few-layer nanosheets, the optical absorption is blue-shifted with respect to that of the bulk due to quantum confinement effects [16, 17]. The MoS_2 has potential applications in supercapacitors, photocatalytic processes as hydrogen production, or removal of organic pollutants and heavy metals from waste water [18–21]. To obtain the benefits of electronic properties of MoS_2 exfoliated and expand the optical absorption edge of TiO_2 to a solar spectrum, the TiO_2-MoS_2 heterostructures have been synthesized using nanobelts, hollow spheres, and nanofibers using TiO_2 as template by the hydrothermal technique obtaining improvement in the photocatalytic activity and hydrogen production as compared with the use of only TiO_2 or MoS_2 [16, 22, 23]. On the other hand, the MoS_2 has a high adsorption capacity for organic molecules presented in a dye solution [20]. The fast adsorption of molecules from colored solution on the MoS_2 surface happens in the dark phase of adsorption-desorption between photocatalysist and dye solution, previous to light irradiation. However, the organic dye molecules are only adsorbed on the surface of the MoS_2 and have not been degraded, because the catalyst has not been activated yet and the electron-hole pairs has not been generated to carry on the oxidation-reduction reactions. The adsorption of the dyes on MoS_2 could be eliminated if we deposited a layer on this material, which has the characteristics of not adsorbing the dyes. If this material also has the characteristics of being a good photocatalyst (as TiO_2), it would have an important effect on photodegradation. Hočevar et al. reported the preparation of a thin layer of TiO_2 using a Pechini sol-gel method [24]. In the present work, we fabricated a TiO_2-MoS_2/TiO_2 film from MoS_2 nanosheets deposited on TiO_2 nanofibers and covered with a thin layer of TiO_2. We studied the role that plays the thin TiO_2 layer on adsorption and photocatalytic process on the degradation of rhodamine B (RhB) solution under visible-infrared light irradiation.

2. Materials and Methods

The used materials were as follows: PVP (polyvinylpyrrolidone 1,300,000 wt.) from Alfa Aesar; anhydrous ethanol, titanium (IV) isopropoxide 97%, glacial acetic acid, sodium molybdate 98%, thiourea 99% and hydrochloric acid 37%, citric acid 99.5%, and anhydrous ethylene glycol 99.8% from Sigma-Aldrich; and bidistilled water from J.T. Baker.

2.1. Fabrication of TiO_2 Nanofibers. A 13% wt. solution of PVP in anhydrous ethanol was prepared as polymeric solution. The TiO_2 precursor solution was prepared as follows: 1.546 ml of titanium (IV) isopropoxide, 1.905 ml of acetic acid, and 1.270 ml of anhydrous ethanol were mixed and stirred on a magnetic plate for 10 minutes. The TiO_2 precursor solution was added dropwise into polymeric solution and left to stir for 3 h at room temperature for a complete homogenization of the mixture. The TiO_2 polymeric solution was transferred to 5 ml syringe with a stained steel needle of 0.7 mm inner diameter and injected from a syringe pump at 1 ml/h. The distance between needle tip and collector was of 8 cm, and 14 kV was applied to electrospun the polymeric solution. The nanofibers obtained were annealed at 600°C with a heating ramp of 10°C/min, for 5 h under a nitrogen atmosphere to eliminate the organic compounds and crystallize the TiO_2.

2.2. Synthesis of MoS_2 Nanosheets and TiO_2-MoS_2 Heterostructures. The MoS_2 nanosheets were synthetized by a hydrothermal technique as follows: 9.43 g of sodium molybdate and 8.67 g of thiourea were dissolved into 30 ml double distilled water to form a transparent solution and stirred vigorously for 10 min on a magnetic plate, then drops of a 12 M of HCl solution were added until reaching a $pH \leq 1$. The dark blue solution was transferred to a Teflon-lined stainless steel autoclave and heated at 200°C for 24 h. The black precipitate was washed several times with double distilled water, dried at 100°C for 12 h, and grounded until a fine powder was obtained. To synthetize the TiO_2-MoS_2 heterostructures, 0.5 g of annealed TiO_2 nanofibers previously synthetized was added into the MoS_2 precursor solution described above and sonicated for 30 min following the same process.

2.3. Fabrication of TiO_2-MoS_2/TiO_2 Films. The first step in the preparation of the TiO_2-MoS_2/TiO_2 films was the synthesis of a Pechini solution based on a titanium sol. The TiO_2 Pechini solution was prepared from a titanium isopropoxide/citric acid/ethylene glycol solution with a molar ratio of 1 : 4 : 16, respectively. The sol was prepared by mixing of ethylene glycol and titanium isopropoxide into a volumetric flask then heating to 85°C and stirring for 1 h. Finally, citric acid was added and the solution was stirred at this temperature until it turned clear. The second step was the preparation of the mix of TiO_2-MoS_2 powder and the TiO_2 sol as follows: the TiO_2-MoS_2 powder was dissolved into 2 ml of anhydrous ethanol and sonicated for 2 h; then, an amount of TiO_2 sol was added and sonicated for 3 hours; the alcohol in excess was extracted. The molar ratio between the TiO_2-MoS_2 powder and the TiO_2 sol in the mix formulation was 1 : 1. The mix was deposited on a 2.5 cm × 2.5 cm glass substrate, using the spin-coating technique at 1500 rpm for 60 s. Layers were annealed at 450°C for one hour under argon flow. In order to understand the role played by the TiO_2 layer in the adsorption and photocatalytic process, a Pechini solution without the titanium precursor was prepared to deposit the MoS_2 and TiO_2-MoS_2 films without TiO_2 layer. For easy identification, the samples were labeled as follows: MoS_2 without TiO_2 layer (MF), TiO_2-MoS_2 without TiO_2 layer (TMF), MoS_2 with TiO_2 layer (MTF), and TiO_2-MoS_2 with TiO_2 layer (TMTF). Figure 1 shows a scheme of process followed to prepare the heterostructures.

3. Characterization Techniques

The morphology of the heterostructure was studied by a Field Emission-Scanning Electron Microscope (FE-SEM) from (Zeiss, Auriga), operating at 1 kV using the in-lens detector.

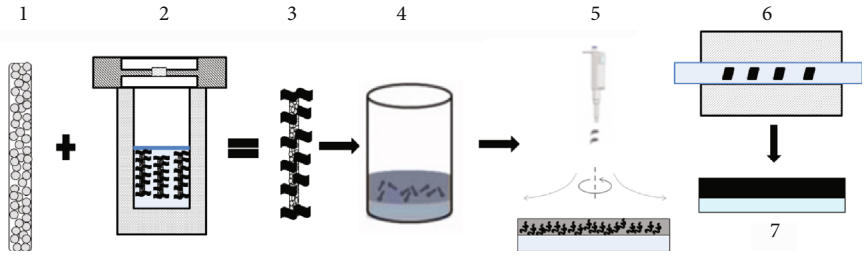

Figure 1: Scheme of process followed to prepare the heterostructures. 1: synthesis of TiO_2 nanofibers by electrospinning, 2: synthesis of TiO_2-MoS_2 by a hydrothermal technique, 3: TiO_2-MoS_2 composite, 4: TiO_2-MoS_2+TiO_2 Pechini solution, 5: spin-coating deposition, 6: thermal annealed, and 7: the TiO_2-MoS_2/TiO_2 heterostructure.

The topography of film was collected from a JSPM-2500 Scanning Probe Microscope of JEOL in tapping mode on the surface of $1.5\,\mu \times 1.5\,\mu$. A high resolution transmission electron microscope (HR-TEM) was carried out with a transmission electron microscope JEOL model JEM-ARM200F operated at 200 kV. The X-ray diffraction (XRD) patterns were collected with an X-ray diffractometer using the CuKα radiation (D8 ECO, Bruker). All samples were analyzed at 40 KV and 40 mA, in the range of 10 to 70° 2-theta degrees with a step size of 0.05° and a step time of 1 s. The diffuse reflectance spectroscopy and the absorption spectra were collected by an Ocean Optics spectrophotometer model USB4000-XR1-ES coupled to UV/Vis/NIR light source model DH-2000. The N_2 adsorption isotherms were carried out with an ASAP 2050 Micrometrics; the samples were activated to 130°C for 6 h; this condition was supplied from the TGA thermogram. In order to understand the effect of the TiO_2 layer over the MoS_2, the TMTF sample, before and after the degradation experiment, was characterized by means of X-ray photoelectron spectroscopy (XPS) (model K alpha by Thermo Scientific). The general survey as well as the high resolution spectra in the regions of the C 1s, O 1s, Ti 2p, S 2p, and Mo 3d was obtained at the surface of the films. The binding energy of the C 1s line at 284.5 eV was taken as the reference peak to calibrate the obtained spectra.

3.1. Photocatalysis Test. The photocatalytic test was performed on discoloration of 80 ml of Rh B solution, with a concentration of 5 mg/l, placed into a 100 ml quartz reactor with a water recirculation system. The irradiation source was provided by a 100 W halogen lamp with a range of 350 nm to 2500 nm (USHIO, USA). The power lamp was modulated by a SORENSEN variable power supply, in order to have wavelengths longer than 400 nm. We found that using a 11.5 V and 7.6 A, the wavelengths were in the range required in the experiment. The samples were vertically placed around the reactor walls and radial irradiated with 87.4 W for 6 h. The residual concentration (C/Co) of Rh B solution was monitored by the variation intensity of the absorption band at 551 nm. Before to the photocatalyst test, the photolysis reaction between the Rh B solution and light source was carried out for 3 h; after that, the dye solution was stirred in the dark for one hour to reach the adsorption-desorption equilibrium. The adsorption-desorption test was performed in the same conditions of the photocatalysis test but in the absence of light for 6 h.

4. Results and Discussion

4.1. Morphological and Crystallinity Structure Analysis. Figure 2(a) shows the SEM image of pure MoS_2; as synthetized, a sphere with a diameter around of 2-3 μm can be observed, with the nanosheets growing perpendicularly to the surface. The image of TiO_2-MoS_2 heterostructures is shown in Figure 2(b); it is observed that a few layers of MoS_2 nanosheets have grown vertically around the TiO_2 nanofibers surface; the diameter of TiO_2 nanofibers was around 250 nm. The superficial TiO_2 grains of the nanofibers form defects that interact with the metallic precursors. In a way, nucleation centers were created that allow the growth of MoS_2 exfoliated nanosheets on the surface of the TiO_2 nanofibers [8]. Figure 2(c) shows the TMTF sample; in the film, the TiO_2-MoS_2 composite was covered with a thin layer of TiO_2; we can observe that film surface has some clusters and cracks produced for the annealing. From the AFM image of Figure 2(d), it is observed that the surface of TMTF is formed for several clusters of material that cause a high roughness. The horizontal and vertical profile graph inside the AFM image confirms the wide height difference between the cluster; also, some cluster separations between them due to the cracks caused by annealing also observed in the SEM image are observed.

Figure 3(a) shows the HRTEM image of the sample TMT; TEM image reveals that the heterostructure was formed for polycrystalline TiO_2 grains and MoS_2 monolayers stacked to form nanosheets deposited onto the TiO_2 surface. From the HAADF image, Figure 3(b), it is observed that the MoS_2 nanosheets were small, their size was around 11 nm wide and 33.2 nm for length, and the distance between monolayers was around 0.69 nm. The FFT (Fast Fourier Transform) inside the HAADF images shows that crystals in the inner of the nanofiber were TiO_2 rutile covered for TiO_2 anatase crystals and the MoS_2 nanosheets formed for around 11 monolayers according to the ICDS cards 202242, 165921, and 24000 for anatase, rutile, and MoS_2-2H molybdenite, respectively.

The XRD patterns of the MTF and TMTF are shown in Figure 3. The XRD pattern of the MTF (Figure 4(a)) exhibits the characteristic diffraction peaks of molybdenite-2H, corresponding to the planes (002), (101), (103), and (110) matched with ICSD-24000. A low intensity TiO_2 diffraction peak at 25.2° was detected; this could be related to the thin layer that coverages the surface of MoS_2 on the film. The

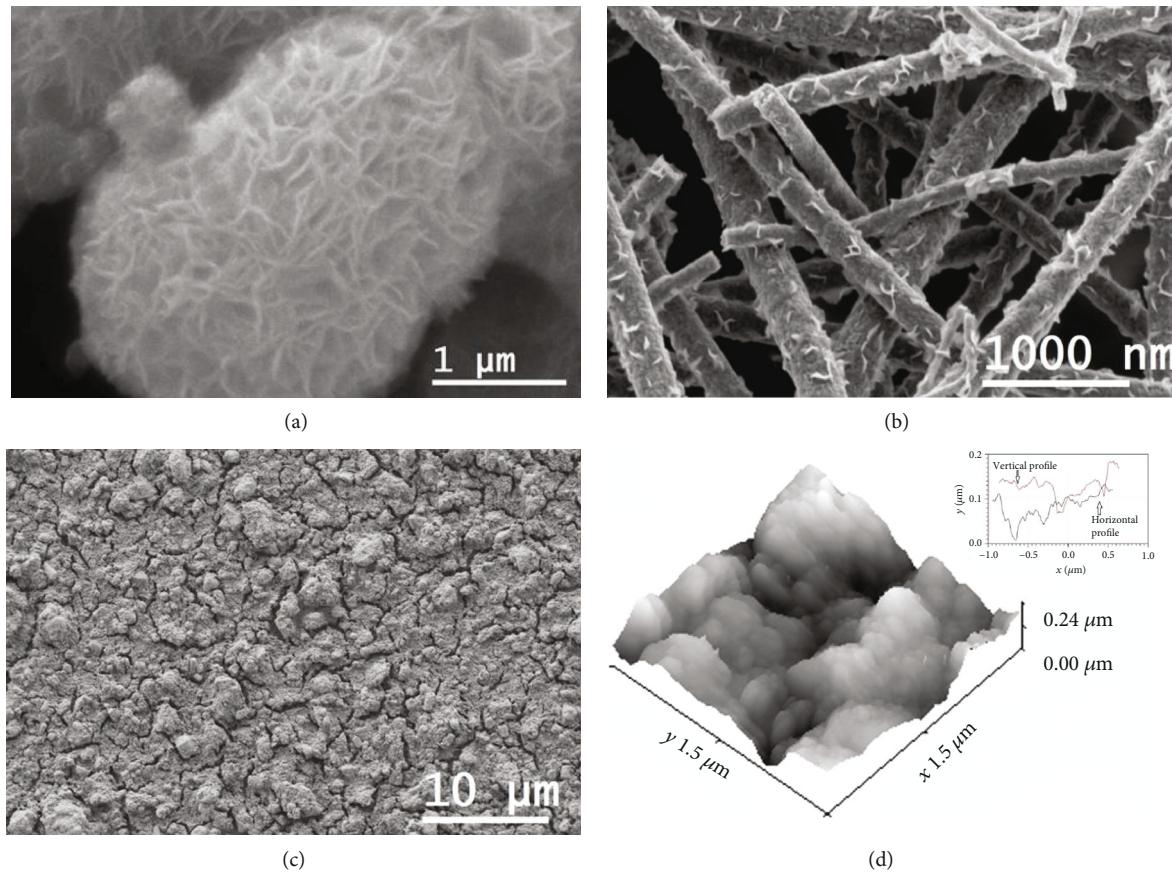

(a) (b) (c) (d)

Figure 2: SEM images of the as-prepared (a) MoS_2, (b) TiO_2-MoS_2 heterostructure, and (c) low magnification of TMTF surface; (d) tapping mode AFM image of TMTF, inside them horizontal and vertical profile graph of surface.

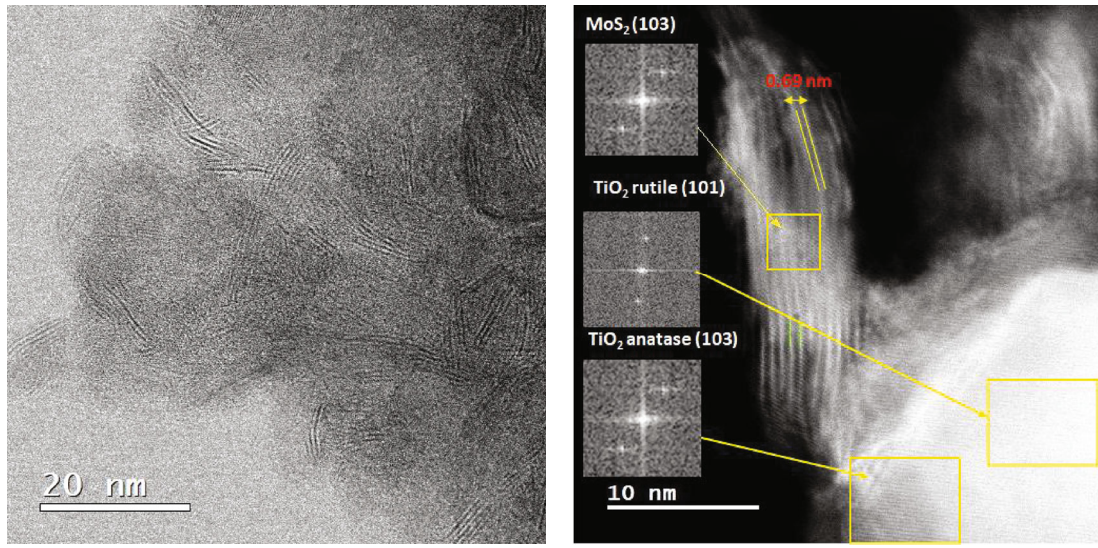

(a) (b)

Figure 3: HR-TEM image of (a) TiO_2-MoS_2 heterostructure and (b) HAADF image for TiO_2-MoS_2 heterostructure, inside FFT images for MoS_2, TiO_2 rutile, and anatase.

diffraction peak at 14.05° corresponds to the "C" axis of the MoS_2; the intensity of this peak is related to the amount of layers stacked in the structure of MoS_2. A monolayer of MoS_2 is composed of Mo atoms coordinated with S atoms to form the S-Mo-S laminated layer [22]. The XRD pattern of the TMTF (Figure 4(b)) shows diffraction peaks assigned

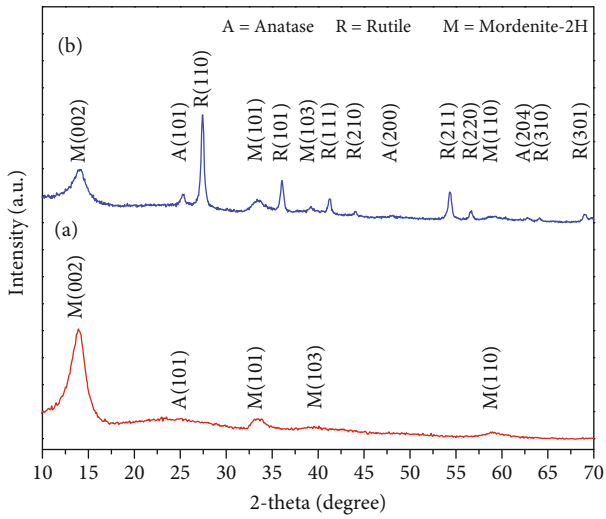

Figure 4: XRD diffractograms of (a) MTF and (c) TMTF after annealed to 450°C.

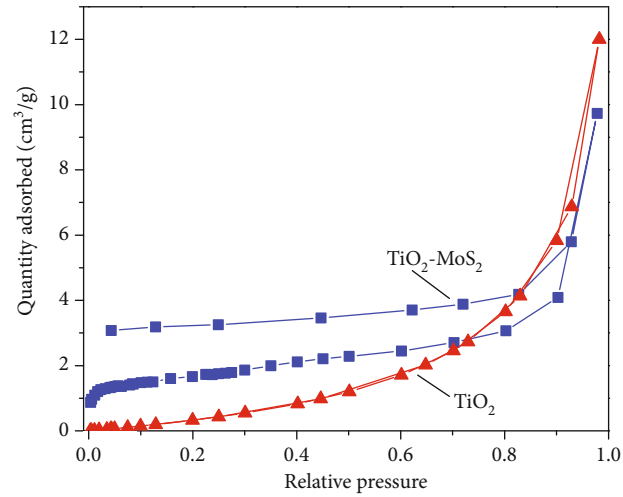

Figure 5: N_2 adsorption isotherms for TiO_2 nanofibers and TiO_2-MoS_2.

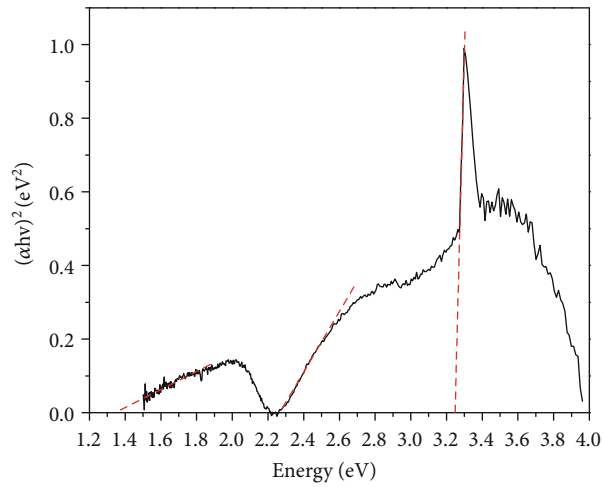

Figure 6: Tauc plot of TMTF sample.

to TiO_2 or MoS_2. The diffraction peaks of MoS_2 have the same position as in the MTF. The diffraction peak at 14.05° is less intense than in the MTF suggesting that the heterostructure is composed for a few monolayers of MoS_2 [25], which are what give rise to the nanosheets according to observations in Figure 2(a). Most of TiO_2 diffraction peaks were matched to rutile phase corresponding to the planes (110), (101), (111), (210), (211), (220), (310), and (301) according to ICSD-165921. The presence of rutile is due to the influence of gas used in the annealing of TiO_2 nanofibers as observed in previous work [26]. Few weak anatase diffraction peaks were observed corresponding to the planes (101), (200), and (204) according to the ICSD-202242. The anatase reflection is from the TiO_2 thin layer that coverages the surface of the heterostructure.

The nitrogen adsorption-desorption isotherms of the TiO_2 nanofibers and TiO_2-MoS_2 heterostructures, Figure 5, were used to estimate the BET surface area. The TiO_2 nanofibers show a greater specific surface area (19.9 m^2/g) than that of TiO_2-MoS_2 heterostructure; when the MoS_2 nanosheets grew up on the TiO_2 nanofiber surface, the specific surface area reduces to 7.87 m^2/g because the pores in TiO_2 nanofibers were occupied with MoS_2 nanosheets. Additionally, both materials are mesoporous structure; this result is consistent with that reported by Liu et al. [16].

4.2. Optical Properties. The band gap energy (E_g) values of TMTF were determined through diffuse reflectance spectroscopy, plotting the $[\alpha(h\nu)h]^2$ vs. photon energy ($h\nu$) axis and extrapolating the linear portion of the absorption edge to zero [27]. Figure 6 shows the Tauc plot for the TMTF is possible to note three optical adsorption edges at 1.3 eV, 2.28 eV, and 3.23 eV. The first one (1.3 eV) is due to the presence of MoS_2 bulk. The second one (2.25 eV) maybe related to quantum confinement due to nanosheet exfoliation as observed in the TEM image; Quinn et al. obtained MoS_2-exfoliated monolayers with a band gap of 1.97 eV [28]; it can also be related to the formation of electronic traps between the heterostructure junctions. The last one (3.23 eV) corresponds to the TiO_2 anatase layer that coverages the surface of film.

4.2.1. X-Ray Photoelectron Spectroscopy. In order to investigate the formation and the stability of the external layer of TiO_2, the sample TMTF was characterized before and after the degradation experiment. The chemical composition and chemical state were identified with the help of XPS analysis; the binding energy of the peaks were obtained from XPS database of NIST [29]. The XPS spectra of the TMTF sample: (a) survey, (b) Ti 2p, (c) S 2p, and (d) Mo 3d, are shown in Figures 7(a)–7(d). From Figure 7(a), the elements S, Mo, C, Ti, and O are observed in the XPS survey spectrum, which confirms the formation of the superficial TiO_2 layer; the presence of Mo and S elements is related to the MoS_2 intermediate layer, and the thickness of the TiO_2 overlayer is less than 10 nm. In Figure 7(b), the high resolution spectra of Ti 2p is presented; a doublet is observed with one peak related to Ti $2p_{3/2}$ and the other to Ti $2p_{1/2}$ with binding energies of

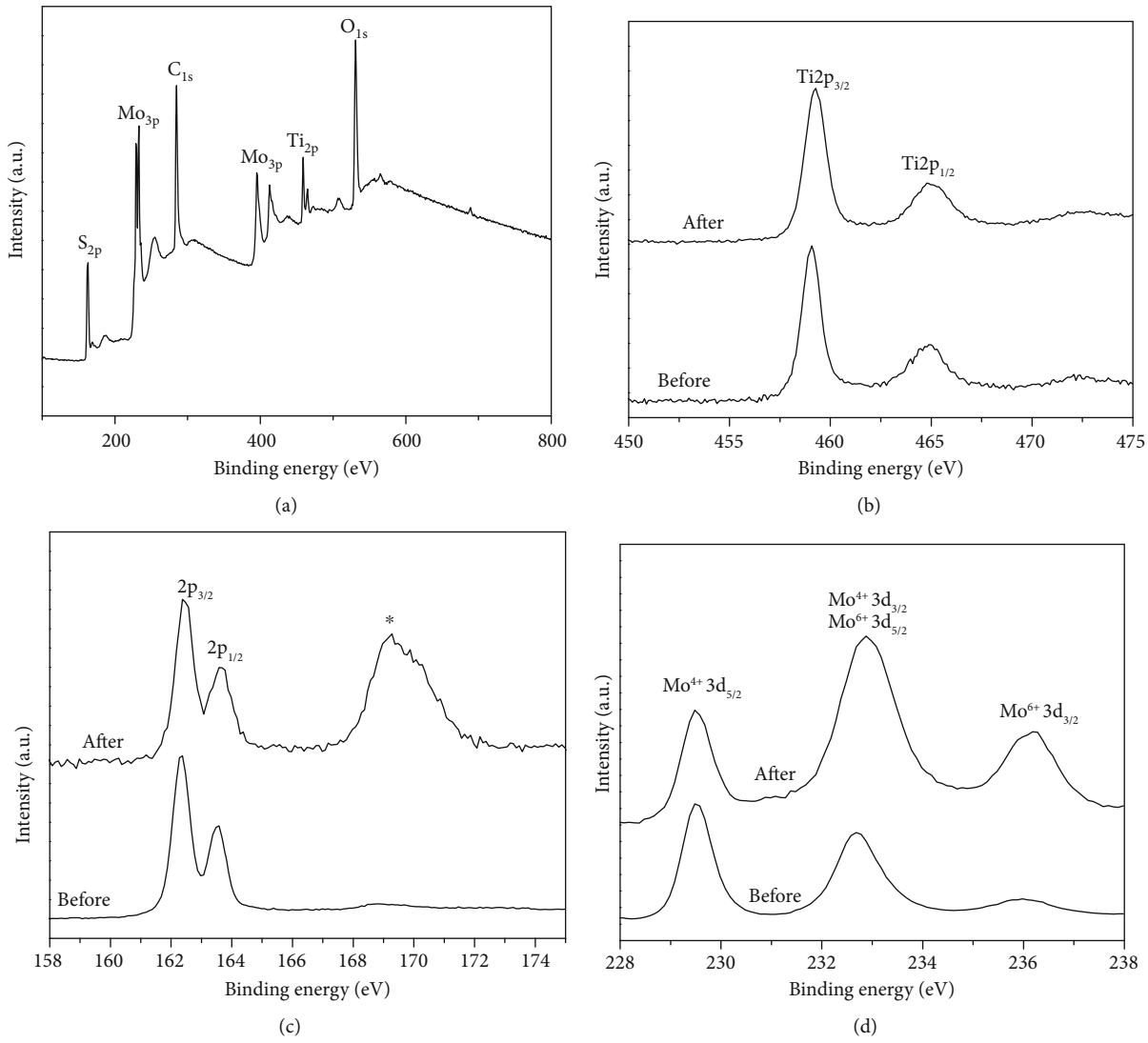

Figure 7: XPS spectra of TMTF sample (a) general survey, (b) high resolution of Ti 2p, (c) high resolution of S 2p, and (d) high resolution Mo 3d. The label before and after means before and after photocatalytic experiment.

459.0 eV and 464.7 eV, respectively. The binding energies found are related to the Ti with the chemical environment of TiO_2. It can be observed that the peaks presented stability after the degradation experiment, suggesting that our external layer is stable. The high resolution spectra of the S 2p is presented in Figure 7(c); the presence of a doublet related to S $2p_{3/2}$ and S $2p_{1/2}$ at binding energies of 162.3 eV and 163.6 eV, respectively, can be seen. After the photodegradation experiment, additional peak appears at a binding energy of 169 eV (labeled in the figure with *); the presence of this peak had been reported previously [30, 31] in TiO_2 doped with S; this peak disappears after the sample was eroded with argon ions. The presence of this peak could be related to the fact that we deposited a thin layer of precursor solution of TiO_2 over MoS_2; then, a thermal annealing was applied at the sample and a sulfur diffusion on TiO_2 was promoted. Hence, the peak could be due to the binding of sulfur with the adsorbed dye in the surface of the sample, and when we eroded with argon ions, we eliminated the adsorbed dye and the peak disappears. The high resolution spectrum of Mo 3d (Figure 7(d)) can be separated into two doublets. The first doublet at 229.6 eV and 232.7 eV is related to Mo $3d_{5/2}$ and Mo $3d_{3/2}$, related to Mo^{4+} of the MoS_2 compound; the second at 233.4 eV and 236.5 eV is related to Mo $3d_{5/2}$ and Mo $3d_{3/2}$, related to Mo^{6+} of the MoO_3 compound. Similar results had been reported by Senthil et al. [32].

4.3. Photocatalytic Activity. The aim of this work is to evaluate the effect of the TiO_2 thin layer over the MoS_2; then, it has been evaluated on the adsorption-desorption capacity and their photocatalysis activity on the degradation of Rh B solution in the dark and Vis-IR light, respectively. Figure 8 shows the variation of residual concentration (C/Co) with the time of the Rh B solution in the dark in the presence of the films. The films without a TiO_2 thin layer coating in the surface of heterostructure, MF and TMF, show that the adsorption-desorption equilibrium between the photocatalyst and the dye solution is not reached after 6 h. The constant

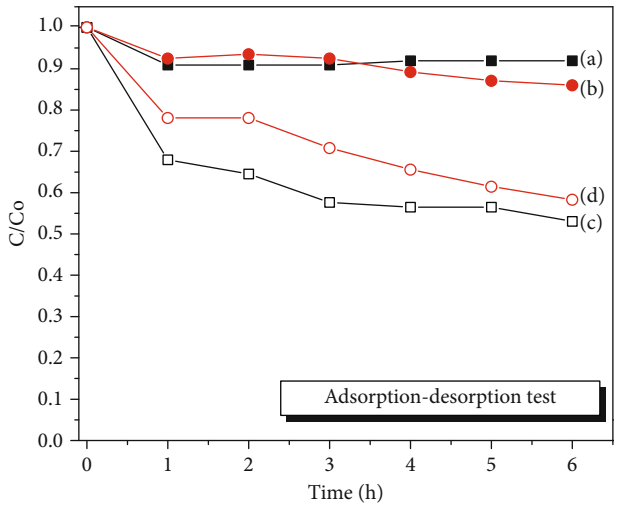

(a) MTF
(b) TMTF
(c) MF
(d) TMF

Figure 8: Adsorption-desorption test between Rh B solution in the presence of different photocatalyst. The test was carried out in the dark.

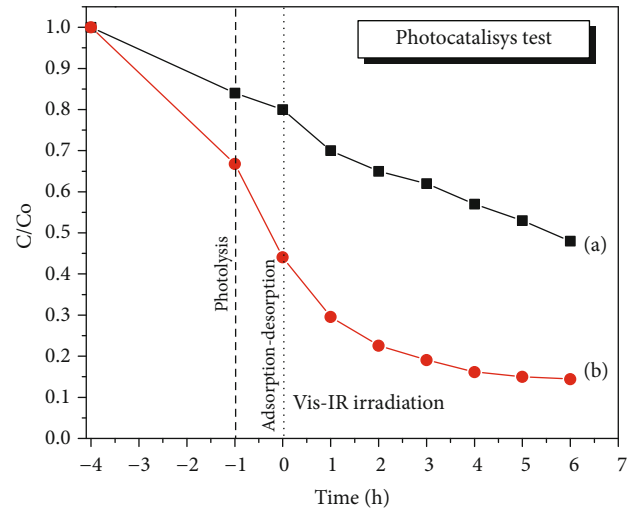

(a) MTF
(b) TMTF

Figure 9: Photocatalytic test between Rh B solution in the presence of different photocatalyst. The test was carried out under Vis-IR light.

discoloration in the dark of the dye solution is due to the MoS_2 as 2D-layered nanomaterials that had excellent anchoring surface for adsorbing dye molecules [33]. But the Rh B molecules are being superficially adsorbed on MoS_2, and not necessarily degraded. After 6 h of contact, about 50% of solution was discolored for both samples. Instead with the films coating with a TiO_2 thin layer, MTF and TMTF were placed in contact to dye solution in the dark; the adsorption-desorption equilibrium was reached in the first hour, and the concentration of Rhodamine B solution remained constant after 6 h. The obtained result indicates that the TiO_2 thin layer coating the heterostructure decreases drastically the adsorption capacity of MoS_2. Now, the adsorption of organic molecules is carried out on the TiO_2 surface.

Figure 9 shows the photocatalysis degradation of Rh B solution in the presence MTF and TMTF under Vis-IR light irradiation. The variation of residual concentration (C/Co) with the time is observed. The TMTF shows a better photocatalytic activity; it is related to the band gap energy; the TMTF shows an absorption edge in the visible and near-infrared; then, the catalyst is photoactive in a larger region of the solar spectrum. Additionally, the high roughness of TMTF as observed in AFM images provides more contact surface to interact with the dye solution. After 6 h of irradiation, the 90% of Rh B solution was degraded for the TMTF. Taking into account that the discoloration of Rh B solution produced by the photolysis and adsorption effect were made before the irradiation, all discoloration of dye during the photocatalysis test is due to oxidation-reduction reaction between photocatalyst and organic molecules from dye solution.

Liu et al. [7] determined the band alignment for the TiO_2/multilayer MoS_2 interfaces; they report the valence band offset (VBO) and conduction band offset (CBO) of TiO_2/ML-MoS_2 interfaces were 2.28 eV and 0.28 eV, respectively. A possible process for photogeneration electron-hole pairs and the transfers between TiO_2 and MoS_2 into the heterostructure is described below, a schematic illustration is shown in Figure 10.

(1) The photons from the Vis-IR light are absorbed by the MoS_2, generating the electron-hole pairs

(2) When the energy of electrons in CBO is bigger than 0.28 between MoS_2 and TiO_2, the electron in the conduction band (CB) of MoS_2 is transmitted to the CB of the TiO_2

(3) An electron from the CB of TiO_2 is displaced and reacts with oxygen to produce superoxide anion radicals

(4) Simultaneously, the electrons from the valence band (VB) of TiO_2 absorb the energy needed to overcome the VBO between TiO_2 and MoS_2 and compensate the electronic vacancy in the VB of MoS_2

(5) The hole generated in the VB of TiO_2 reacts with rhodamine B and is degraded

A possible mechanism for RhB degradation by the TiO_2-MoS_2/TiO_2 composites includes the possible steps listed below. The enhanced photocatalytic performance of the TiO_2-MoS_2/TiO_2 composites could result from the charge transfer process between MoS_2 and TiO_2. Under Vis-IR light irradiation, electrons and hole pairs were produced on MoS_2 of CB and VB, respectively (equation (1)). When the MoS_2 electrons have an energy bigger than the CBO, the electron in the conduction band (CB) of MoS_2 is transmitted to the CB of the TiO_2 (equation (2)). The electrons on the conduction band of TiO_2 react with adsorbed O_2 on the surface of the photocatalysts and produce superoxide radical ($\dot{O}_2^-$) to

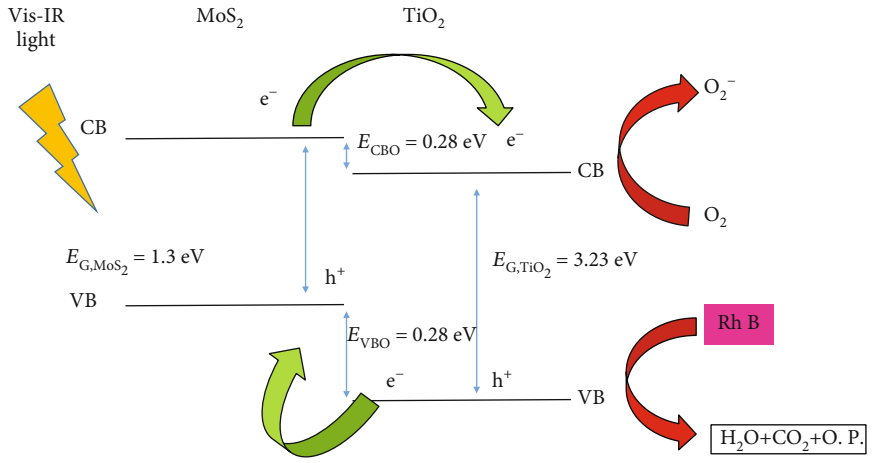

FIGURE 10: Schematic illustration of charge transfer of TiO_2-MoS_2/TiO_2 film in the visible-infrared light.

oxidize RhB (equation (3)). On the other hand, when the electrons from the valence band (VB) of TiO_2 absorb the energy needed to overcome the VBO between TiO_2 and MoS_2 and compensate the electronic vacancy in the VB of MoS_2 and generated a hole (h^+) in the VB of TiO_2 (equation (4)), the (h^+) generated in the VB of TiO_2 reacts with the rhodamine B producing an oxidized $RhB^{+\cdot}$ that in the presence of O_2 dissolved in water is reduced to rhodamine as intermediate (equations (5) and (6)); other (h^+) from VB of TiO_2 dissociates the H_2O in $OH^{\cdot}$ and H^+ (equation (7)); simultaneously, the RhB reaction with the $^{\cdot}O_2$- or $^{\cdot}OH$ or H^+ generated from other reactions to finally produce carbon dioxide and water (equations (8) and (9)).

$$MoS_2 + hv_{(Vis-IR)} \longrightarrow MoS_2(e^-) + MoS_2(h^+) \quad (1)$$

$$MoS_2(e^-) + TiO_2 \longrightarrow MoS_2 + TiO_2(e^-) \quad (2)$$

$$TiO_2(e^-) + O_2 \longrightarrow O_2^{-\cdot} + TiO_2 \quad (3)$$

$$2TiO_2 + hv_{(VBO)} + MoS_2(h^+) \longrightarrow MoS_2 + TiO_2(h^+) \quad (4)$$

$$TiO_2(h^+) + RhB \longrightarrow RhB^{+\cdot} + TiO_2 \quad (5)$$

$$RhB^{+\cdot} + O_2 \longrightarrow Rhodamine \quad (6)$$

$$H_2O + TiO_2(h^+) \longrightarrow OH^{\cdot} + H^+ + TiO_2 \quad (7)$$

$$RhB + O_2^{\cdot -}/{}^{\cdot}OH \longrightarrow Products \quad (8)$$

$$RhB + H^+ \longrightarrow CO_2 + H_2O + other\ products \quad (9)$$

5. Conclusions

The thin layer of TiO_2 that coverages the MoS_2 and TiO_2-MoS_2 to form the heterostructure film practically eliminate the strong adsorption capabilities of the MoS_2 in the dark. The heterostructures show excellent photocatalytic activities under visible to infrared light illumination. The photocatalysis activity was superior to MoS_2/TiO_2 film. The heterostructures might have promising applications in polluted water treatment and facile recovery to reuse.

Data Availability

The XRD, DRS, and SEM, XPS, AFM, TEM images and absorbance spectra data used to support the findings of this study are available from the corresponding author upon request.

Conflicts of Interest

The authors declare that there is no conflict of interests regarding the publication of this paper.

Acknowledgments

The authors want to acknowledge to the Research and Postgraduate Secretary of Instituto Politécnico Nacional for the financial support by the project SIP-IPN (20190155).

References

[1] X. Liu, B. Liu, L. Li et al., "$Cu_2In_2ZnS_5$/Gd_2O_2S:Tb for full solar spectrum photoreduction of Cr(VI) and CO_2 from UV/vis to near-infrared light," *Applied Catalysis B: Environmental*, vol. 249, pp. 82–90, 2019.

[2] B. Liu, X. Liu, J. Liu et al., "Efficient charge separation between UiO-66 and $ZnIn_2S_4$ flowerlike 3D microspheres for photoelectronchemical properties," *Applied Catalysis B: Environmental*, vol. 226, pp. 234–241, 2018.

[3] C. B. Almquist and P. Biswas, "Role of synthesis method and particle size of nanostructured TiO_2 on its photoactivity," *Journal of Catalysis*, vol. 212, no. 2, pp. 145–156, 2002.

[4] M. Andersson, L. Österlund, S. Ljungström, and A. Palmqvist, "Preparation of nanosize anatase and rutile TiO_2 by hydrothermal treatment of microemulsions and their activity for photocatalytic wet oxidation of phenol," *The Journal of Physical Chemistry. B*, vol. 106, no. 41, pp. 10674–10679, 2002.

[5] A. Sclafani and J. M. Herrmann, "Comparison of the photoelectronic and photocatalytic activities of various anatase and rutile forms of titania in pure liquid organic phases and in

aqueous solutions," *The Journal of Physical Chemistry*, vol. 100, no. 32, pp. 13655–13661, 1996.

[6] J. Li, X. Xu, X. Liu, W. Qin, M. Wang, and L. Pan, "Metal-organic frameworks derived cake-like anatase/rutile mixed phase TiO_2 for highly efficient photocatalysis," *Journal of Alloys and Compounds*, vol. 690, pp. 640–646, 2017.

[7] X. Liu, L. Chen, Q. Liu et al., "Band alignment of atomic layer deposited TiO_2/multilayer MoS_2 interface determined by _x_ -ray photoelectron spectroscopy," *Journal of Alloys and Compounds*, vol. 698, pp. 141–146, 2017.

[8] Z. Zhang, C. Shao, L. Zhang, X. Li, and Y. Liu, "Electrospun nanofibers of V-doped TiO_2 with high photocatalytic activity," *Journal of Colloid and Interface Science*, vol. 351, no. 1, pp. 57–62, 2010.

[9] J. Xu, Y. Ao, D. Fu, and C. Yuan, "A simple route for the preparation of Eu, N-codoped TiO_2 nanoparticles with enhanced visible light-induced photocatalytic activity," *Journal of Colloid and Interface Science*, vol. 328, no. 2, pp. 447–451, 2008.

[10] Y. Yang, C. Zhang, Y. Xu, H. Wang, X. Li, and C. Wang, "Electrospun Er:TiO_2 nanofibrous films as efficient photocatalysts under solar simulated light," *Materials Letters*, vol. 64, no. 2, pp. 147–150, 2010.

[11] N. Qin, Y. Liu, W. Wu et al., "One-dimensional CdS/TiO2Nanofiber composites as efficient visible-light-driven photocatalysts for selective organic transformation: synthesis, characterization, and performance," *Langmuir*, vol. 31, no. 3, pp. 1203–1209, 2015.

[12] Z. Chen, J. Zhao, X. Yang et al., "Fabrication of TiO_2/WO_3 composite nanofibers by electrospinning and photocatalystic performance of the resultant fabrics," *Industrial and Engineering Chemistry Research*, vol. 55, no. 1, pp. 80–85, 2016.

[13] J. Li, X. Xu, X. Liu et al., "Sn doped TiO_2 nanotube with oxygen vacancy for highly efficient visible light photocatalysis," *Journal of Alloys and Compounds*, vol. 679, pp. 454–462, 2016.

[14] J. Li, X. Xu, X. Liu, W. Qin, and L. Pan, "Novel cake-like N-doped anatase/rutile mixed phase TiO_2 derived from metal-organic frameworks for visible light photocatalysis," *Ceramics International*, vol. 43, no. 1, pp. 835–840, 2017.

[15] S.-M. Paek, H. Jung, M. Park, J. K. Lee, and J. H. Choy, "An inorganic nanohybrid with high specific surface area: TiO_2-pillared MoS_2," *Chemistry of Materials*, vol. 17, no. 13, pp. 3492–3498, 2005.

[16] C. Liu, L. Wang, Y. Tang et al., "Vertical single or few-layer MoS_2 nanosheets rooting into TiO_2 nanofibers for highly efficient photocatalytic hydrogen evolution," *Applied Catalysis B: Environmental*, vol. 164, pp. 1–9, 2015.

[17] T. Li and G. Galli, "Electronic properties of MoS_2 nanoparticles," *Journal of Physical Chemistry C*, vol. 111, no. 44, pp. 16192–16196, 2007.

[18] K. J. Huang, L. Wang, Y. J. Liu et al., "Layered MoS_2-graphene composites for supercapacitor applications with enhanced capacitive performance," *International Journal of Hydrogen Energy*, vol. 38, no. 32, pp. 14027–14034, 2013.

[19] J. C. Tokash and B. E. Logan, "Electrochemical evaluation of molybdenum disulfide as a catalyst for hydrogen evolution in microbial electrolysis cells," *International Journal of Hydrogen Energy*, vol. 36, no. 16, pp. 9439–9445, 2011.

[20] X. Bai, J. Wan, J. Jia et al., "Simultaneous photocatalytic removal of Cr(VI) and RhB over 2D MoS_2/red phosphorus heterostructure under visible light irradiation," *Materials Letters*, vol. 222, pp. 187–191, 2018.

[21] Z. Ren, X. Liu, Z. Zhuge, Y. Gong, and C. Q. Sun, "$MoSe_2$/ZnO/ZnSe hybrids for efficient Cr(VI) reduction under visible light irradiation," *Chinese Journal of Catalysis*, vol. 41, no. 1, pp. 180–187, 2020.

[22] W. Zhou, Z. Yin, Y. du et al., "Synthesis of few-layer MoS2 nanosheet-coated TiO_2 nanobelt heterostructures for enhanced photocatalytic activities," *Small*, vol. 9, no. 1, pp. 140–147, 2013.

[23] J. Wang, B. Wei, L. Xu, H. Gao, W. Sun, and J. Che, "Multilayered MoS_2 coated TiO_2 hollow spheres for efficient photodegradation of phenol under visible light irradiation," *Materials Letters*, vol. 179, pp. 42–46, 2016.

[24] M. Hočevar, U. O. Krašovec, M. Berginc, and M. Topič, "One step preparation of TiO_2 layer for high efficiency dye-sensitized solar cell," *Acta Chimica Slovenica*, vol. 57, no. 2, pp. 405–409, 2010.

[25] K. Chang and W. Chen, "Single-layer MoS2/graphene dispersed in amorphous carbon: towards high electrochemical performances in rechargeable lithium ion batteries," *Journal of Materials Chemistry*, vol. 21, no. 43, pp. 17175–17184, 2011.

[26] N. Cruz-González, J. L. Fernández Muñoz, M. Zapata-Torres, and M. García-Hipólito, "Efecto del gas utilizado en el tratamiento térmico y la impurificación con Eu en las propiedades estructurales de nanofibras de TiO_2 depositadas por electrohilado," *Superficies y vacío*, vol. 26, no. 3, pp. 111–116, 2013.

[27] M. Nowak, B. Kauch, and P. Szperlich, "Determination of energy band gap of nanocrystalline SbSI using diffuse reflectance spectroscopy," *Review of Scientific Instruments*, vol. 80, no. 4, p. 046107, 2009.

[28] M. D. J. Quinn, N. H. Ho, and S. M. Notley, "Aqueous dispersions of exfoliated molybdenum disulfide for use in visible-light photocatalysis," *ACS Applied Materials & Interfaces*, vol. 5, no. 23, pp. 12751–12756, 2013.

[29] http://srdata.nist.gov/XPS/.

[30] X. Yang, C. Cao, L. Erickson, K. Hohn, R. Maghirang, and K. Klabunde, "Photo-catalytic degradation of rhodamine B on C-, S-, N-, and Fe-doped TiO_2 under visible-light irradiation," *Applied Catalysis B: Environmental*, vol. 91, no. 3–4, pp. 657–662, 2009.

[31] S. A. Bakar and C. Ribeiro, "Prospective aspects of preferential {001} facets of N,S-co-doped TiO_2 photocatalysts for visible-light-responsive photocatalytic activity," *RSC Advances*, vol. 6, no. 92, pp. 89274–89287, 2016.

[32] R. A. Senthil, S. Osman, J. Pan, Y. Sun, T. R. Kumar, and A. Manikandan, "A facile hydrothermal synthesis of visible-light responsive $BiFeWO_6$/MoS_2 composite as superior photocatalyst for degradation of organic pollutants," *Ceramics International*, vol. 45, no. 15, pp. 18683–18690, 2019.

[33] T. F. Jaramillo, K. P. Jorgensen, J. Bonde, J. H. Nielsen, S. Horch, and I. Chorkendorff, "Identification of active edge sites for electrochemical H_2 evolution from MoS_2 nanocatalysts," *Science*, vol. 317, no. 5834, pp. 100–102, 2007.

Hindawi
International Journal of Photoenergy
Volume 2019, Article ID 6307858, 9 pages
https://doi.org/10.1155/2019/6307858

Research Article

Construction of Direct Z-Scheme Photocatalyst by $Mg_{1.2}Ti_{1.8}O_5$ and g-C_3N_4 Nanosheets toward Photocatalytic H_2 Production and Disinfection

Sijia Gu,[1] Dan Zhang,[1] Shirong Luo,[1] and Heng Yang[2]

[1]*Affiliated Huidong Hospital of Guangdong Medical University, Guangdong Medical University, Huizhou 516300, China*
[2]*Key Laboratory of Pesticide & Chemical Biology of Ministry of Education, College of Chemistry, Central China Normal University, Wuhan 430070, China*

Correspondence should be addressed to Heng Yang; ccnu_yh@sina.com

Received 15 September 2019; Accepted 11 November 2019; Published 1 December 2019

Guest Editor: Muhammad S. Javed

Exploring a novel and efficient photocatalyst is the key research goal to relieve energy and environmental issues. Herein, Z-scheme heterojunction composites were successfully fabricated by loading g-C_3N_4 nanosheets (CN) on the surface of $Mg_{1.2}Ti_{1.8}O_5$ nanoflakes (MT) through a simple sol-gel method followed by the calcination method. The crystalline phase, morphologies, specific surface area, and optical and electrochemical performance of the samples were characterized by X-ray diffraction (XRD), field emission scanning electron microscopy (FE-SEM), energy-disperse X-ray spectroscopy (EDS), Brunauer-Emmett-Teller (BET), diffuse reflectance spectroscopy (DRS), and electrochemical measurements. Considering the suitable band structures of the components, the photocatalytic performance was evaluated by photocatalytic H_2O splitting and photocatalytic inactivation of Escherichia coli (E. coli). Among the samples, MT/CN-10 (the molar percentage of melamine to as-obtained Mg-Ti gel was 10%) shows superior photocatalytic performance, which the average H_2 production rate was 3.57 and 7.24 times higher than those of MT and CN alone. Additionally, the efficiency of inactivating Escherichia coli (E. coli) over MT/CN-10 was 1.95 and 2.06 times higher as compared to pure MT and CN, respectively. The enhancement of the photocatalytic performance was attributed to the advantages of the extremely negative conduction band (CB) of CN and the extremely positive valence band (VB) of MT, the enhanced light absorption, and more efficient photogenerated charge carrier separation.

1. Introduction

During the past decade, there is an increasing interest in addressing the problem related to the growing concentration of energy shortage and other related damaging environmental pollutions due to the combustion of the fossil fuels [1–3]. Under the circumstances, developing advanced technologies is very urgent, which are able to reduce the use of fossil fuels and exploit the renewable and environmentally friendly energy sources [4–6]. Photocatalytic technology is a promising approach towards solving the above problems, which can transform H_2O into H_2 and relieve the environmental pollution under solar light irradiation. Thus, considerable research efforts have been made to develop efficient photocatalysts for the usage of photocatalytic hydrogen production and disinfection due to the technology advantage of convenient and environmentally friendly operation process and no harmful disinfection by-products, such as metal oxide and sulfide, as well as metal chloride semiconductors [7–11]. Lately, perovskite as a semiconductor photocatalyst for water splitting has become a research hotspot. Compared with the most studied metal oxides and sulfides, the perovskite shows a more suitable conduction band position and higher stability, as well as abundant light absorption. Magnesium titanate, as a member of the perovskite family, has been reported to be an efficient photocatalyst of water splitting to product hydrogen and the degradation of pollutants. However, pure perovskite has two major drawbacks, namely, low surface area and high recombination rate of photogenerated electron hole pairs [12–15]. Therefore, to enhance the photocatalytic efficiency,

the strategy of designing effective artificial photosynthetic systems by mimicking the Z-scheme mechanism in the chloroplast has been developed. Graphitic carbon nitride (g-C_3N_4), as a metal-free polymeric semiconductor with a narrow bandgap of about 2.7 eV, has been widely studied among various semiconductors in view of its low cost, nontoxicity, good thermal and chemical stability, and higher reduction potential position [16–22]. However, the poor separation efficiency of photogenerated charge carriers and insufficient light absorption of bulk g-C_3N_4 directly synthesized by the thermal polycondensation method would lead to inferior performance and limitation of application [23–28]. Given that of these shortcomings, constructing the Z-scheme heterostructure by recombining g-C_3N_4 with perovskite has been regarded as an ideal solution to expand the specific surface area and restrain the recombination of photogenerated charges.

Herein, we have successfully synthesized the Z-scheme heterojunction photocatalyst consisting of $Mg_{1.2}Ti_{1.8}O_5$ nanosheets (MT) and g-C_3N_4 nanosheets (CN) by the sol-gel method and calcination method. The photocatalytic performance was evaluated by photocatalytic water splitting and disinfection under simulated sunlight irradiations. Compared with pure $Mg_{1.2}Ti_{1.8}O_5$ and g-C_3N_4, the Z-scheme heterojunction photocatalyst exhibited excellent photocatalytic activity by taking the advantages of the more negative conduction band (CB) of CN, the more positive valence band (VB) of MT, the enhanced light absorption, and more efficient photogenerated charge carrier separation.

2. Experimental Section

2.1. The Preparation of Photocatalyst. All chemicals used in this work were analytical grade without any further purification. The heterojunction composite composed of g-C_3N_4 and $Mg_{1.2}Ti_{1.8}O_5$ was obtained by the sol-gel method and ionothermal method. In a typical sol-gel preparation procedure, 0.03 mol of acetic acid was poured into 0.16 mol absolute ethanol to form a transparent solution, and then 0.01 mol of $Ti(OC_4H_9)_4$ was dropped into the above solution with constantly stirring to form transparent solution. After that, 0.01 mol of $Mg(NO_3)_2{\cdot}6H_2O$ was slowly added into the above solution to generate homogeneous yellow sol. Finally, the above yellow sol was dried in air to obtain Mg-Ti gel. Additionally, in the process of ionothermal calcination method, a certain amount of melamine was mixed with the as-obtained Mg-Ti gel at molar ration of 5%, 10%, and 20%, respectively. Then, the above mixture (1.0 g) was mixed with KCl (2.75 g) and LiCl (2.25 g). After being mixed evenly, the resultant mixture was transferred into a corundum crucible and calcined at 550°C for 2 h with a heating rate of 5°C/min in a muffle furnace. The resultant product was washed with boiling distilled water and then followed by drying at 60°C overnight in a vacuum oven. By way of comparison, pure g-C_3N_4 and $Mg_{1.2}Ti_{1.8}O_5$ were also prepared using the similar procedure. The synthetic samples were labeled as CN, MT, MT/CN-5, MT/CN-10, and MT/CN-20, respectively.

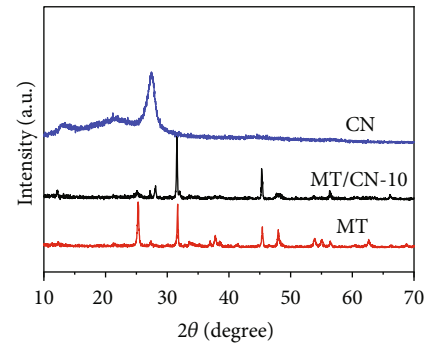

Figure 1: XRD patterns of pure CN, MT, and MT/CN-10 Z-scheme heterojunction photocatalyst.

2.2. Characterizations. The X-ray diffraction (XRD) patterns were recorded on a Bruker D8 Advance instrument with Cu-Kα as the radiation source. The morphologies of the as-obtained samples were characterized by a JSM-7500 field emission scanning electron microscope (FE-SEM). The specific surface area and pore structure were analyzed by N_2 adsorption-desorption isotherms using a Micromeritics ASAP 2020 Apparatus (Micromeritics Instruments, USA). The optical performance of samples was characterized by a UV-visible spectrophotometer (UV-2600, Shimadzu, Japan). Room temperature photoluminescence (PL) emission spectra of the samples were collected on a Hitachi F-700 fluorescence spectrophotometer at an excitation wavelength of 325 nm. Electrochemical measurements were carried out on an electrochemical workstation (CHI66E, China) with a standard three-electrode cell, where Na_2SO_4 solution as the electrolyte, Pt foil acted as the counter electrode, and Ag/AgCl (saturated KCl) as the reference electrode.

2.3. Evaluation of Photocatalytic Hydrogen Evolution. The photocatalytic hydrogen evolution was evaluated on a Labsolar-6A system (Pefect Light Company, Beijing China), where a 300 W Xenon arc lamp was used as simulated sunlight source. In the process of photocatalytic water splitting, circulating cooling water system is used to guarantee that the temperature of reaction system be kept at 25 ± 1°C. Firstly, 50 mg of the as-prepared photocatalyst was dispersed in 80 ml of triethanolamine (TEOA) aqueous solution (10 vol%). Then, a certain amount of H_2PtCl_6 aqueous solution was dripped into the system to load 1.0 wt% Pt onto the surface of the photocatalyst by a photochemical reduction deposition method. After illumination for 1 h under magnetic stir, 0.4 ml of the produced gas was automatically withdrawn and injected into the gas chromatograph (GC-2014C, Shimazu, Japan) to determine the concentration of the produced H_2 gas.

2.4. Photocatalytic Disinfection Experiment. The photocatalytic performance of the obtained samples was evaluated by the inactivation of Escherichia coli (E. coli). Firstly, in order to obtain the inoculum, the bacteria was incubated in 100 ml Luria-Bertani (LB) nutrient solution and shaken at 37°C for 12 h, and then centrifuged to remove the metabolites.

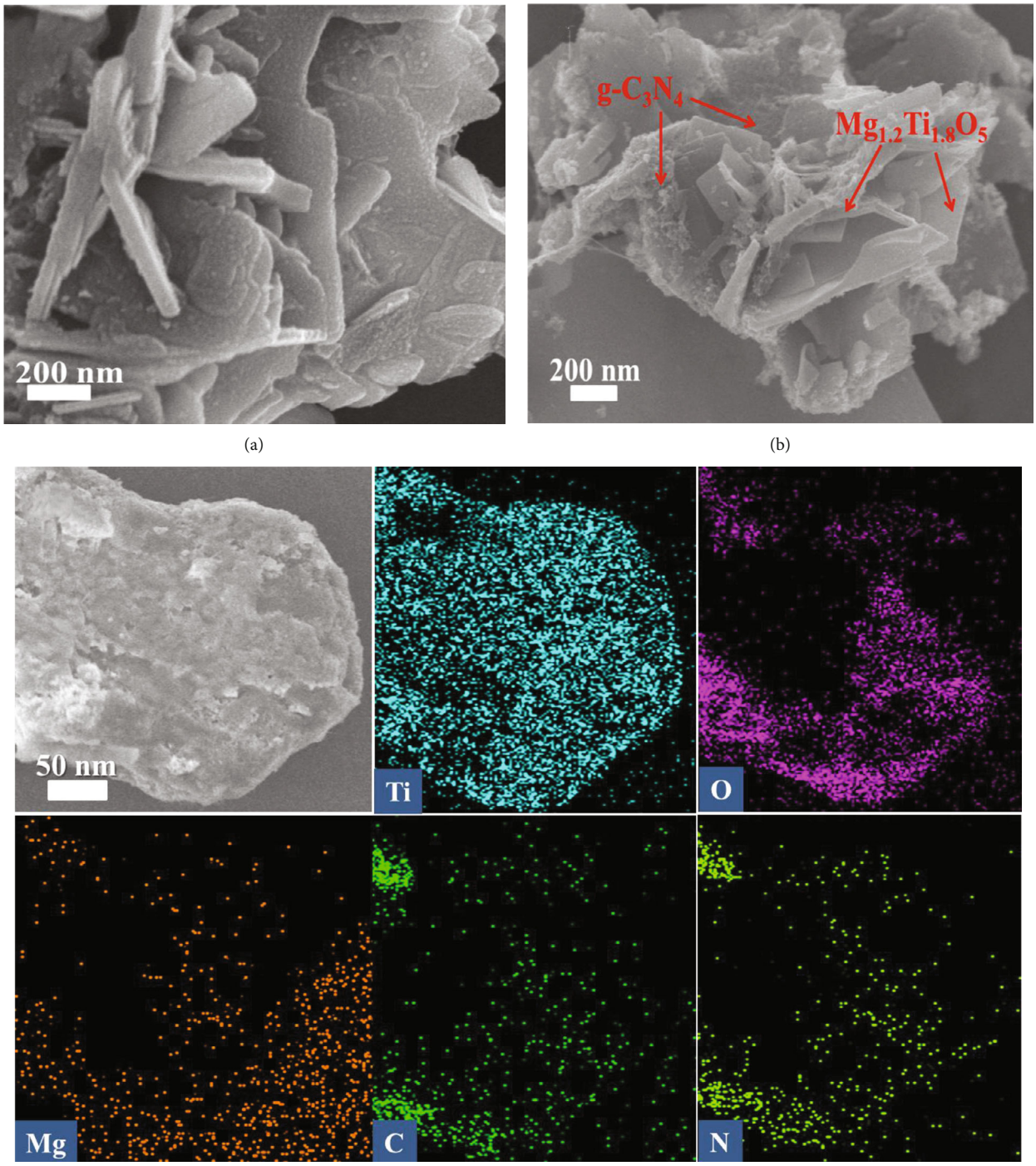

Figure 2: (a) FE-SEM images of pure MT. (b) MT/CN heterojunction. (c) SEM-EDS element mapping analysis of the MT/CN heterojunction.

Subsequently, the bacterial cell pellet was washed twice with sterilized saline (0.9% NaCl) solution and then resuspended in the sterilized saline solution. The obtained bacteria cell density was about 5×10^7 colony forming units per milliliter (CFU/ml). Finally, the photocatalytic disinfection experiment was carried out. Namely, 30 ml of E. coli suspension was mixed with 20 mg photocatalyst powder and stirred at 500 rpm for 5 min in the dark. A 300 W Xenon lamp with an AM1.5 filter was employed as the simulated sunlight source to irradiate the E. coli cells. At regular intervals, aliquots were taken from the suspension buffer and 0.1 ml of the suspension (undiluted, three replicates) was spread onto LB agar plates, and then incubated at 37°C for 18 h to form viable colony units. All inactivation experiments were performed in triplicate, and all glassware was heated at 120°C for 20 min in an autoclave to ensure the sterility.

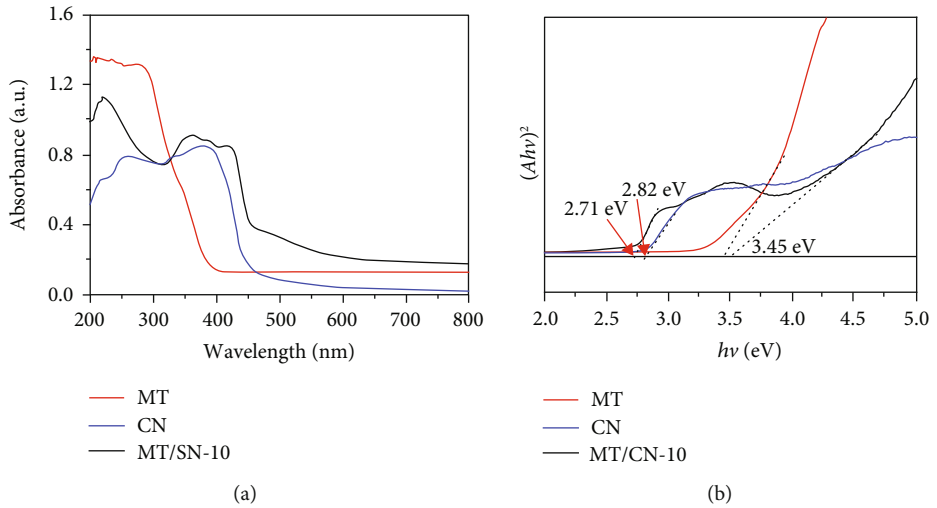

Figure 3: (a) UV-Vis absorption spectra and (b) the bandgap evaluation from the (αhv) [2] photon energy plots for CN, MT/CN-10, and MT samples.

3. Results and Discussion

The XRD patterns of the synthesized CN, MT, and MT/CN-10 composite are shown in Figure 1. It can be observed that the two typical diffraction peaks of CN appeared at 27.5° and 13.1° are classified to (002) and (100) diffraction planes, which are assigned to the interlayer stacking of aromatic segments and in-plane structural packing motif of tri-s-triazine units [29–31]. The pure MT exhibits five stronger diffraction peaks at 2θ of 25.5°, 32.1°, 39.6°, 45.4°, and 48.2°, corresponding to the (110), (023), (113), (043), and (200) facets, respectively [12]. After the introduction of CN into the MT, the heterojunction sample reveals characteristic diffraction peaks for both CN and MT without any position shifts, indicating the coexistence of these two components in the heterojunctions.

The field emission scanning electron microscope (FE-SEM) measurement was carried out to characterize the morphologies and structures of MT and MT/CN samples. As shown in Figure 2(a), the pristine MT displays the aggregated structure consisting of several two-dimensional (2D) sheets with a thickness of 10–20 nm. By contrast, the image of MT/CN composite shows that many CN nanoparticles grow on the surface of the 2D MT nanosheets (Figure 2(b)). The microstructure of the MT/CN composite was further explored by SEM-EDS elemental mapping measure. The elemental mapping images reveal C, N, Ti, and O, and Mg elements are well-distributed in the composite (Figure 2(c)). Those abovementioned results further proved that the MT/CN heterojunction was successfully synthesized.

The optical absorption properties of the obtained samples were investigated by UV-vis diffuse reflectance measurement. As shown in Figure 3(a), steep adsorption band edge of pure MT is observed in the ultraviolet region, whereas an obvious adsorption edge which can be assigned to the intrinsic bandgap absorption of pure CN is approximately located at 450 nm. Remarkably, the adsorption band edge of the MT/CN-10 heterojunction photocatalyst exhibits a red shift in comparison to that of pristine CN and MT, implying that the enhanced light absorption ability would be highly conducive to boost the photocatalytic performance. Moreover, the optical bandgap energy can be calculated by the following equation [32, 33]:

$$\alpha hv = A\left(hv - E_g\right)^{n/2}, \quad (1)$$

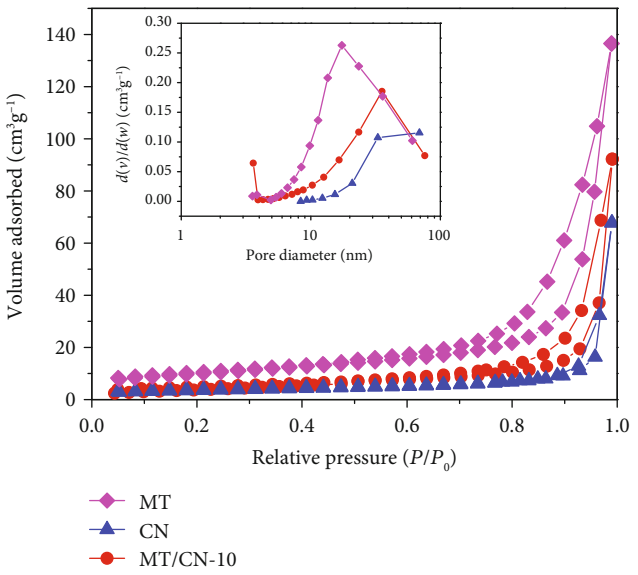

Figure 4: The N_2 adsorption-desorption isotherms and pore size distributions (inset of the figure).

Table 1: Physicochemical properties of MT, CN, and MT/CN-10 composite.

Sample	S_{BET} ($m^2\ g^{-1}$)	Cumulative volume of pores ($cm^3\ g^{-1}$)	Average pore diameter (nm)
MT	34.7	0.21	24.1
CN	12.1	0.10	34.4
MT/CN-10	20.9	0.15	31.5

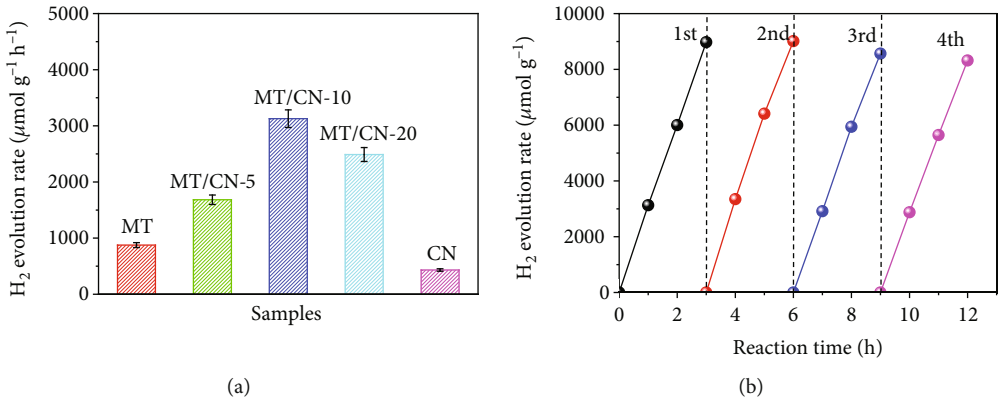

FIGURE 5: (a) Comparison of H_2 generation rate of as-prepared samples under Xenon lamp irradiation (full spectrum), with photodeposition of 1% Pt as cocatalyst. (b) Time courses of photocatalytic H_2 generation amount of MT/CN-10.

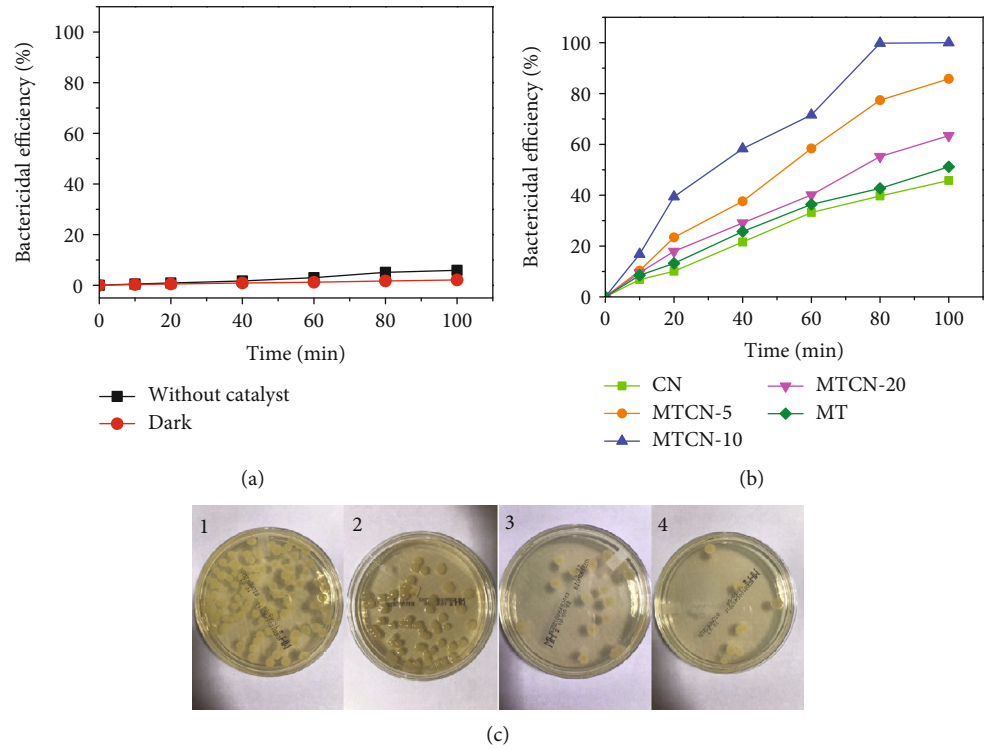

FIGURE 6: (a) Inactivation efficiency against E. coli by photocatalyst in the dark and without photocatalyst under simulated solar light. (b) The inactivation of E. coli by as-prepared photocatalysts under simulated solar light. (c) Photographs of colonies formed by E. coli cells in water samples after treated by MT/CN-10 suspensions with simulated solar light for 0 (c1), 20 (c2), 60 (c3), and 80 (c4) min.

where A, α, $h\nu$, and E_g represent a constant, the absorption coefficient, the photon energy, and the optical bandgap, respectively. In this equation, n is determined by the transition type. The bandgap energies of the MT and CN are determined from a plot of $(\alpha h\nu)$ [2] versus $h\nu$ ($n = 1$ for direct transition). Thus, the bandgaps of MT and CN are estimated to 3.45 eV and 2.71 eV, respectively (Figure 3(b)).

The adsorption-desorption curves and pore volume distribution curves of MT, CN, and MT/CN-10 composite are shown in Figure 4. And the corresponding calculated results of BET surface area are also listed in Table 1. Obviously, all samples exhibit the type IV isotherms with type H3 hysteresis loops [34, 35], which are characteristics of slit-like pores formed by the stacking of nanosheets. However, after combining CN with the MT, the specific surface area and pore volume of MT/CN composite distinctly decreased as compared to that of pure MT, which might attributed to the fact that the small CN nanosheets filled or blocked large numbers of micropores of MT.

The photocatalytic performance of the obtain catalysts was evaluated by photocatalytic hydrogen production under simulated solar light irradiation. Figure 5(a) depicts the photocatalytic H_2 evolution rate of various photocatalysts. The results showed that the H_2 evolution rate firstly increased and then decreased with the increasing loading amount of CN. The MT/CN-10 in particular outperforms (3128.3 μmol/h/g)

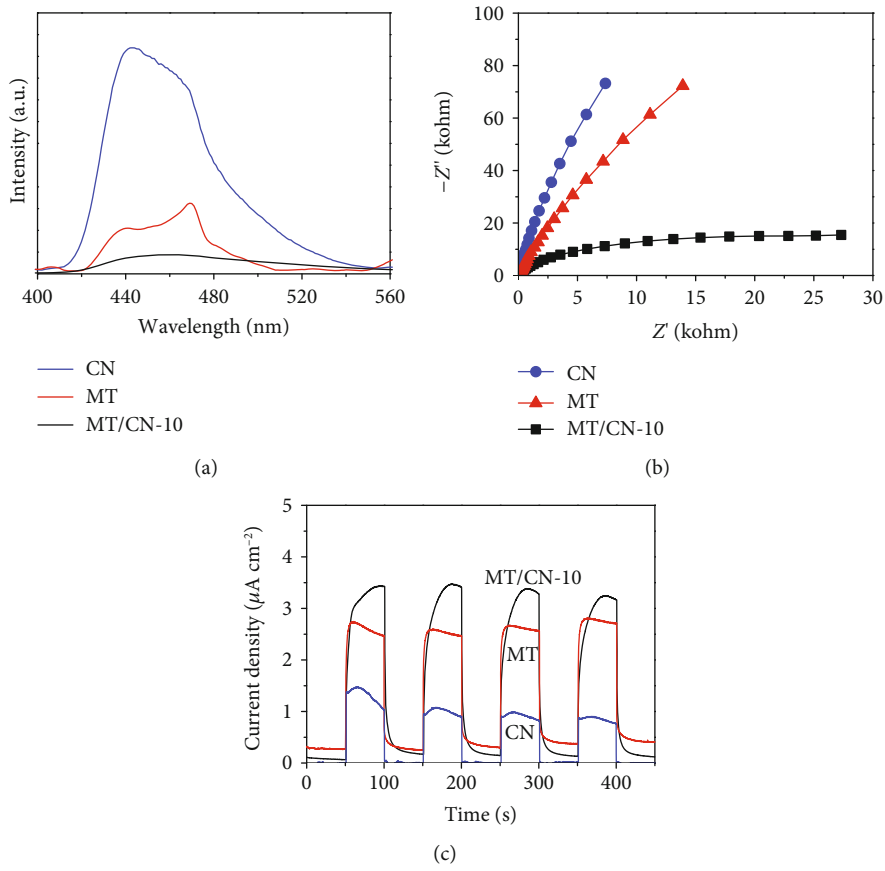

Figure 7: (a) Steady-state photoluminescence spectrum (PL) of samples (excitation wavelength of 325 nm). (b) Nyquist plots of electrochemical impedance spectra (EIS) for samples. (c) Transient photocurrent-time profiles for samples.

among all the photocatalysts, which was about 3.57 and 7.24 times higher than that of pure MT and CN, respectively. The stability and reusability of the photocatalyst is of great significance to its practical application. Figure 5(b) demonstrates no significant decrease in the photocatalytic H_2 production amount of MT/CN-10 after four repetitive cycles, indicating that MT/CN-10 possesses high photocatalytic stability and recyclability. Moreover, in order to assess the enhanced photocatalytic efficiency of MT/CN composites, the inactivation efficiencies of the E. coli over the as-prepared samples were also investigated in Figure 6. Compare the photocatalytic disinfection efficiencies of different samples under simulated solar light irradiation at room temperature and ambient pressure as well as the blank one with photocatalyst (MT/CN-10 sample alone) but under dark condition. In parallel, the inactivation efficiency of the E. coli without adding any photocatalysts was also evaluated. As it can be found in Figure 5(a), the inactivation of the bacteria barely happens in the absence of photocatalyst, and no disinfection efficiency of the E. coli was observed when the photocatalyst (MT/CN-10) is used without light irradiation. In addition, the MT/CN composites exhibit higher inactivation efficiencies than that of pure MT and CN by the simulated solar light illumination. Particularly, almost 100.0% of E. coli can be killed by MT/CN-10 over 100 min of simulated solar light exposure (Figures 6(b) and 6(c)), while the inactivation efficiencies only reach to 51.2% and 48.5% for pure MT and CN after 100 min, respectively. These results demonstrate that the photocatalytic E. coli inactivation activity can be significantly improved by constructing the heterojunction about CN and MT.

To reveal the significant effect of CN on the photocatalytic activity of MT, the photoluminescence (PL), photocurrent responses, and electrochemical impedance spectrum (EIS) analysis were conducted to explore the charge carrier transfer efficiencies of pure MT, CN, and MT/CN-10 composite. Figure 7(a) shows that the PL intensity of MT/CN-10 is the weakest than that of pure MT and CN, and the CN displays the strongest PL intensity, indicating that the recombination of photogenerated charge carriers is effectively inhibited after loading CN on the surface of MT. Furthermore, the enhanced transport of charge carriers can be further evidenced by the lower electric resistance and higher photocurrent response. As shown in Figure 7(b), the MT/CN-10 composite exhibits the smallest hemicycle radius. And the MT/CN-10 hybrid can afford a much enhanced current density than that of the bare MT and CN (Figure 7(c)). These above results further corroborate that the heterojunction between MT and CN can enhance the separation and transfer efficiency of charge carriers, which is beneficial for improving the photocatalytic disinfection performance.

The electronic spin resonance (ESR) measurement was carried out to detect the active radicals [36, 37]. As displayed in Figure 8(a), the DMPO-·OH signal can be observed for pure MT and MT/CN-10, while no DMPO-·OH signal is

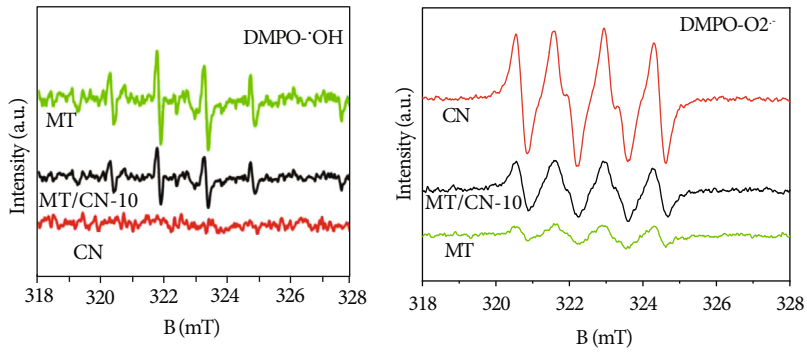

Figure 8: The DMPO spin-trapping ESR spectrum for (a) DMPO-·OH and (b) DMPO-·O_2^- under simulated solar light irradiation.

found for pure CN; this is due to the weak oxidation potential of CN. The strongest DMPO-·OH signal for MT/CN-10 suggests that the photogenerated holes still stay in the valence band (VB). At the same time, the DMPO-·O_2^- signals can be also observed for pure CN and MT/CN-10, but weak DMPO-·O_2^- signal appears in the MT (Figure 8(b)). The results indicate that the photogenerated electrons and holes stay in the conduction band (CB) of CN and the valence band (VB) of MT, respectively. The conventional type II heterojunction mechanism is hard to explain the EPR results. Contrarily, the Z-scheme heterojunction mechanism is more reasonable to explain the enhancement of the photocatalytic H_2 production and disinfection performance.

According to the atom's Mulliken electronegativity definition formula (Equations (2) and (3)) [38, 39],

$$E_{VB} = X - E_0 + 0.5E_g, \quad (2)$$

$$E_{CB} = E_{VB} - E_g, \quad (3)$$

where E_{VB} is the valence band potential, E_{CB} is the conduction band potential, E_g is the semiconductor bandgap energy, E_0 is the electron free energy (in general 4.5 eV), and X is the geometrical mean of the absolute electronegativity of each atom in the semiconductor. Thus, the E_{VB} and E_{CB} of MT are 3.11 V and −0.34 V, whereas the E_{VB} and E_{CB} of CN are 1.59 V and −1.12 V, respectively. To the end, the mechanism of the enhanced disinfection performance for the MT/CN heterojunction composites under simulated solar light irradiation is shown in Figure 9. Under simulated solar light irradiation, the excited electrons transfer from the CB of CN to the CB of MT, and the excited holes transfer from the VB of MT to the VB of CN. Thus, an internal electric field is produced at the interface between CN and MT. Simultaneously, band edge of CN bends upward due to the loss of electrons, but band edge of MT bends downward due to the accumulation of electrons. Under the influence of the internal electric field, the electrons on the CB of MT transfer to the VB of CN and recombine with the holes on the VB of CN. Therefore, more electron hole pairs can be efficiently separated, and more electrons and active radicals are obtained to enhance the photocatalytic H_2 production and disinfection, respectively.

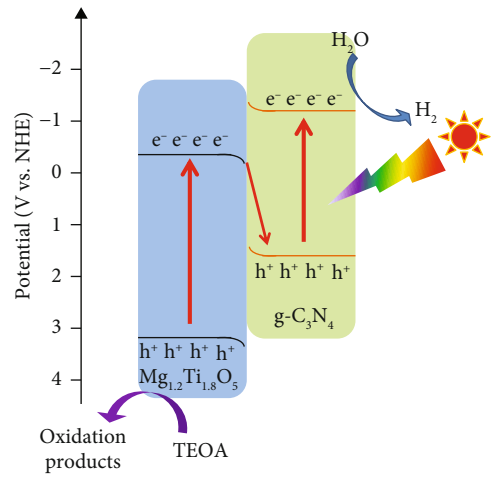

Figure 9: A possible photocatalytic mechanism for H_2 production based on MT/CN heterostructure.

4. Conclusions

In this work, we successfully synthesized a Z-scheme 2D/2D MT/CN heterostructured photocatalyst by a simple sol-gel method followed by calcination method to grow CN nanosheets on the surface of MT nanoflakes. And the MT/CN-10 exhibited much more excellent photocatalytic H_2 production performance and disinfection efficiency than that of pure MT and CN. The establishment of heterojunction between MT and CN can lead a superior interfacial charge transfer under simulated solar light irradiation so as to generate more electrons and active radicals for H_2 production and bacteria inactivation, respectively. In addition, the efficient harvesting of light and the large specific surface area of 2D MT/CN nanosheets are of great importance of the enhancement of the photocatalytic efficiency. These results could provide a new view for the design of heterojunction photocatalysts for applications in solar-to-chemical energy conversion and environmental remediation.

Data Availability

The data used to support the findings of this study are available from the corresponding author upon request.

Conflicts of Interest

The authors declare that there is no conflict of interests regarding the publication of this paper.

Authors' Contributions

Dan Zhang and Shirong Luo contributed equally to this work.

Acknowledgments

This work was supported by the Science and Technology Planning Project of Huizhou (2018Y322).

References

[1] Q. Liu, Y. Xu, J. Wang et al., "Fabrication of Ag/AgCl/$ZnFe_2O_4$ composites with enhanced photocatalytic activity for pollutant degradation and *E. coli* disinfection," *Colloids and Surfaces A: Physicochemical and Engineering Aspects*, vol. 553, no. 20, pp. 114–124, 2018.

[2] M. Mousavi, A. Habibi-Yangjeh, and S. R. Pouran, "Review on magnetically separable graphitic carbon nitride-based nanocomposites as promising visible-light-driven photocatalysts," *Journal of Materials Science: Materials in Electronics*, vol. 29, no. 3, pp. 1719–1747, 2018.

[3] Z. G. Zhao and M. Miyauchi, "Nanoporous-walled tungsten oxide nanotubes as highly active Visible-Light-Driven photocatalysts," *Angewandte Chemie International Edition*, vol. 47, no. 37, pp. 7051–7055, 2008.

[4] R. P. Schwarzenbach, B. I. Escher, K. Fenner et al., "The challenge of micropollutants in aquatic systems," *Science*, vol. 313, no. 5790, pp. 1072–1077, 2006.

[5] D. L. Sedlak and U. von Gunten, "The chlorine dilemma," *Science*, vol. 331, no. 6013, pp. 42-43, 2011.

[6] X. Zeng, Z. Wang, G. Wang et al., "Highly dispersed TiO_2 nanocrystals and WO_3 nanorods on reduced graphene oxide: Z-scheme photocatalysis system for accelerated photocatalytic water disinfection," *Applied Catalysis B: Environmental*, vol. 218, no. 5, pp. 163–173, 2017.

[7] M. Pelaez, N. T. Nolan, S. C. Pillai et al., "A review on the visible light active titanium dioxide photocatalysts for environmental applications," *Applied Catalysis B: Environmental*, vol. 125, no. 21, pp. 331–349, 2012.

[8] M. D. Hernández-Alonso, F. Fresno, S. Suárez, and J. M. Coronado, "Development of alternative photocatalysts to TiO_2: challenges and opportunities," *Energy & Environmental Science*, vol. 2, no. 12, pp. 1231–1257, 2009.

[9] C. A. Castro, A. Jurado, D. Sissa, and S. A. Giraldo, "Performance of Ag-TiO_2 photocatalysts towards the photocatalytic disinfection of water under interior lighting and solar simulated light irradiations," *International Journal of Photoenergy*, vol. 2012, Article ID 261045, pp. 1–10, 2012.

[10] Q. Zhou, S. Ma, and S. Zhan, "Superior photocatalytic disinfection effect of Ag-3D ordered mesoporous CeO_2 under visible light," *Applied Catalysis B: Environmental*, vol. 224, no. 4, pp. 27–37, 2018.

[11] Y. Jia, S. Zhan, S. Ma, and Q. Zhou, "Fabrication of TiO2–Bi2WO6Binanosheet for enhanced solar photocatalytic disinfection ofE. coli: insights on the mechanism," *ACS Applied Materials & Interfaces*, vol. 8, no. 11, pp. 6841–6851, 2016.

[12] N. Zhang, Y. Qu, K. Pan, G. Wang, and Y. Li, "Synthesis of pure phase $Mg_{1.2}Ti_{1.8}O_5$ and $MgTiO_3$ nanocrystals for photocatalytic hydrogen production," *Nano Research*, vol. 9, no. 3, pp. 726–734, 2016.

[13] L. Meng, Z. Ren, W. Zhou, Y. Qu, and G. Wang, "$MgTiO_3$/$MgTi_2O_5$/TiO_2 heterogeneous belt-junctions with high photocatalytic hydrogen production activity," *Nano Research*, vol. 10, no. 1, pp. 295–304, 2017.

[14] Y. Qu, W. Zhou, Y. Xie et al., "A novel phase-mixed $MgTiO_3$–$MgTi_2O_5$ heterogeneous nanorod for high efficiency photocatalytic hydrogen production," *Chemical Communications*, vol. 49, no. 76, pp. 8510–8512, 2013.

[15] X. Zhou, J. Yao, M. Yang et al., "Synthesis of MoSe2/SrTiO3-Heterostructures with enhanced ultraviolet-light-driven and visible-light-driven photocatalytic properties," *Nano*, vol. 13, no. 04, p. 1850038, 2018.

[16] J. Xu, Q. Gao, X. Bai, Z. Wang, and Y. Zhu, "Enhanced visible-light-induced photocatalytic degradation and disinfection activities of oxidized porous g-C_3N_4 by loading Ag nanoparticles," *Catalysis Today*, vol. 332, no. 34, pp. 227–235, 2019.

[17] W. Ong, L. Tan, Y. Ng, S. Yong, and S. Chai, "Graphitic carbon nitride (g-C_3N_4)-based photocatalysts for artificial photosynthesis and environmental remediation: are we a step closer to achieving sustainability?," *Chemical Reviews*, vol. 116, no. 12, pp. 7159–7329, 2016.

[18] G. Mamba and A. K. Mishra, "Graphitic carbon nitride (g-C_3N_4) nanocomposites: a new and exciting generation of visible light driven photocatalysts for environmental pollution remediation," *Applied Catalysis B: Environmental*, vol. 198, no. 5, pp. 347–377, 2016.

[19] Y. Zheng, L. Lin, B. Wang, and X. Wang, "Graphitic carbon nitride polymers toward sustainable photoredox catalysis," *Angewandte Chemie International Edition*, vol. 54, no. 44, pp. 12868–12884, 2015.

[20] Y. Wang, X. Wang, and M. Antonietti, "Polymeric graphitic carbon nitride as a heterogeneous organocatalyst: from photochemistry to multipurpose catalysis to sustainable chemistry," *Angewandte Chemie International Edition*, vol. 51, no. 1, pp. 68–89, 2012.

[21] S. Cao, J. Low, J. Yu, and M. Jaroniec, "Polymeric photocatalysts based on graphitic carbon nitride," *Advanced Materials*, vol. 27, no. 13, pp. 2150–2176, 2015.

[22] K. Liu, J. Li, X. Yan, and W. Shi, "Synthesis of DirectZ-Scheme MnWO4/g-C3N4Photocatalyst with enhanced visible light photocatalytic activity," *Nano*, vol. 12, no. 10, p. 1750129, 2017.

[23] J. Xu, Z. Wang, and Y. Zhu, "Enhanced visible-light-driven photocatalytic disinfection performance and organic pollutant degradation activity of porous g-C3N4Nanosheets," *ACS Applied Materials & Interfaces*, vol. 9, no. 33, pp. 27727–27735, 2017.

[24] M. Wu, J. Yan, X. Tang, M. Zhao, and Q. Jiang, "Synthesis of potassium-modified graphitic carbon nitride with high photocatalytic activity for hydrogen evolution," *ChemSusChem*, vol. 7, no. 9, pp. 2654–2658, 2014.

[25] S. Fang, Y. Xia, K. Lv, Q. Li, J. Sun, and M. Li, "Effect of carbon-dots modification on the structure and photocatalytic activity of g-C_3N_4," *Applied Catalysis B: Environmental*, vol. 185, no. 15, pp. 225–232, 2016.

[26] G. Liao, S. Chen, X. Quan, H. Yu, and H. Zhao, "Graphene oxide modified g-C3N4hybrid with enhanced photocatalytic

capability under visible light irradiation," *Journal of Materials Chemistry*, vol. 22, no. 6, pp. 2721–2726, 2012.

[27] H. Bian, Y. Ji, J. Yan et al., "In situ synthesis of few-layered g-C3N4with vertically aligned MoS2Loading for boosting solar-to-hydrogen generation," *Small*, vol. 14, no. 3, p. 1703003, 2018.

[28] P. Niu, L. Zhang, G. Liu, and H. M. Cheng, "Graphene-like carbon nitride nanosheets for improved photocatalytic activities," *Advanced Functional Materials*, vol. 22, no. 22, pp. 4763–4770, 2012.

[29] Y. N. Li, Z. Y. Chen, M. Q. Wang, L. Z. Zhang, and S. J. Bao, "Interface engineered construction of porous g-C_3N_4/TiO_2 heterostructure for enhanced photocatalysis of organic pollutants," *Applied Surface Science*, vol. 440, no. 15, pp. 229–236, 2018.

[30] J. Fu, B. Zhu, C. Jiang, B. Cheng, W. You, and J. Yu, "Hierarchical porous O-doped g-C3N4with enhanced photocatalytic CO2Reduction activity," *Small*, vol. 13, no. 15, p. 1603938, 2017.

[31] Y. Xia, Z. He, J. Su, Y. Liu, B. Tang, and X. Li, "Fabrication of novel n-$SrTiO_3$/p-BiOI heterojunction for degradation of crystal violet under simulated solar light irradiation," *Nano*, vol. 13, no. 06, p. 1850070, 2018.

[32] S. Zhou, J. Huang, T. Zhang, H. Ouyang, A. Li, and Z. Zhang, "Effect of variation Mn/W molar ratios on phase composition, morphology and optical properties of $MnWO_4$," *Ceramics International*, vol. 39, no. 5, pp. 5159–5163, 2013.

[33] X. Liu, A. Jin, Y. Jia et al., "Synergy of adsorption and visible-light photocatalytic degradation of methylene blue by a bifunctional Z-scheme heterojunction of WO_3/g-C_3N_4," *Applied Surface Science*, vol. 405, no. 31, pp. 359–371, 2017.

[34] Q. Liang, Z. Li, Y. Bai, Z. H. Huang, F. Kang, and Q. H. Yang, "A composite polymeric carbon nitride with in situ formed isotype heterojunctions for highly improved photocatalysis under visible light," *Small*, vol. 13, no. 9, p. 1603182, 2017.

[35] S. Ma, S. Zhan, Y. Jia, Q. Shi, and Q. Zhou, "Enhanced disinfection application of Ag-modified g-C_3N_4 composite under visible light," *Applied Catalysis B: Environmental*, vol. 186, no. 5, pp. 77–87, 2016.

[36] D. Spasiano, R. Marotta, I. Gargano et al., "Kinetic modeling of partial oxidation of benzyl alcohol in water by means of Fe(III)/O_2/UV-solar simulated process," *Chemical Engineering Journal*, vol. 249, no. 1, pp. 130–142, 2014.

[37] Q. Zhao, X. Liu, Y. Xing, Z. Liu, and C. Du, "Synthesizing Bi_2O_3/BiOCl heterojunctions by partial conversion of BiOCl," *Journal of Materials Science*, vol. 52, no. 4, pp. 2117–2130, 2017.

[38] N. Li, H. Teng, L. Zhang, J. Zhou, and M. Liu, "Synthesis of Mo-doped WO3nanosheets with enhanced visible-light-driven photocatalytic properties," *RSC Advances*, vol. 5, no. 115, pp. 95394–95400, 2015.

[39] X. Bai, L. Wang, R. Zong, and Y. Zhu, "Photocatalytic activity enhanced via g-C3N4Nanoplates to nanorods," *Journal of Physical Chemistry C*, vol. 117, no. 19, pp. 9952–9961, 2013.